Impact of Ural Blocking on Winter Warm Arctic–Cold Eurasian Anomalies. Part I: Blocking-Induced Amplification

DEHAI LUO,[a] YIQING XIAO,[a,b,c] YAO YAO,[a] AIGUO DAI,[d,e] IAN SIMMONDS,[f] AND CHRISTIAN L. E. FRANZKE[g,h]

[a] *RCE-TEA, Institute of Atmospheric Physics, Chinese Academy of Sciences, Beijing, China*
[b] *Physical Oceanography Laboratory, Qingdao Collaborative Innovation Center of Marine Science and Technology, Ocean University of China, Qingdao, China*
[c] *Shanxi Meteorological Observatory, Xi'an, China*
[d] *Department of Atmospheric and Environmental Sciences, University at Albany, State University of New York, Albany, New York*
[e] *National Center for Atmospheric Research, Boulder, Colorado*
[f] *School of Earth Sciences, University of Melbourne, Melbourne, Victoria, Australia*
[g] *Meteorological Institute, University of Hamburg, Hamburg, Germany*
[h] *Center for Earth System Research and Sustainability (CEN), University of Hamburg, Hamburg, Germany*

(Manuscript received 26 August 2015, in final form 1 March 2016)

ABSTRACT

In Part I of this study, the impact of Ural blocking (UB) on the warm Arctic–cold Eurasian (WACE) pattern associated with the winter (DJF) arctic sea ice loss during 1979–2013 is examined by dividing the arctic sea ice reduction region into two dominant subregions: the Barents and Kara Seas (BKS) and the North American high-latitude (NAH) region (Baffin and Hudson Bay, Davis Strait, and Labrador Sea). It is found that atmospheric response to arctic sea ice loss resembles a negative Arctic response oscillation with a dominant positive height anomaly over the Eurasian subarctic region. Regression analyses of the two subregions further show that the sea ice loss over the BKS corresponds to the UB pattern together with a positive North Atlantic Oscillation (NAO^+) and is followed by a WACE anomaly, while the sea ice reduction in the NAH region corresponds to a negative NAO (NAO^-) pattern with a cold anomaly over northern Eurasia.

Further analyses reveal that the UB pattern is more persistent during the period 2000–13 (P2) than 1979–99 (P1) because of the reduced middle-to-high-latitude mean westerly winds over Eurasia associated with the intense BKS warming. During P2 the establishment of the UB becomes a slow process because of the role of the BKS warming, while its decay is slightly rapid. In the presence of the long-lived UB that often occurs with the NAO^+, the BKS-warming-induced DJF-mean anticyclonic anomaly is intensified and widened and then expands southward during P2 to amplify the WACE pattern and induce the southward displacement of its cold anomaly and the further loss of the BKS sea ice. Thus, midlatitude Eurasian cold events should be more frequent as the sea ice loss continues over the BKS.

1. Introduction

Over the past decades, the arctic sea ice has undergone a sharp decline (Comiso et al. 2008; Petoukhov and Semenov 2010; Mori et al. 2014; Simmonds 2015). Although the reduction of the overall arctic sea ice is more pronounced in summer than in winter (Serreze et al. 2007), the winter sea ice cover over the Barents and Kara Seas (BKS) has also declined remarkably during the last three decades (Francis and Hunter 2006; Park et al. 2015). It has been found that the winter arctic sea ice decline is associated with the winter arctic warming through enhanced downward infrared (IR) radiation associated with increased air temperature, water vapor, and clouds (Francis et al. 2005; Park et al. 2015), as well as the ice albedo feedback (Screen and Simmonds 2010, 2013b). Other

Corresponding author address: Dr. Dehai Luo, RCE-TEA, Institute of Atmospheric Physics, Chinese Academy of Sciences, Huayanli 40, Chaoyang District, Beijing 100029, China.
E-mail: ldh@mail.iap.ac.cn

Publisher's Note: This article was revised on 9 June 2016 to correct an editing error in the caption of Fig. 16 that appeared when originally published.

DOI: 10.1175/JCLI-D-15-0611.1

possible mechanisms include the increased export of sea ice through the Fram Strait (Kwok et al. 2009), the atmospheric poleward transport of moisture and sensible heat flux (Park et al. 2015), the enhanced inflow of warm waters from adjacent oceans into the Arctic (Spielhagen et al. 2011), and the phase change of the Atlantic multidecadal oscillation (AMO) (Peings and Magnusdottir 2014).

In the recent decade, extreme cold events have occurred frequently over the Eurasian continents (Zhang et al. 2012; Tang et al. 2013; Mori et al. 2014). The presence of a midlatitude cold anomaly over a region in Eurasia corresponds to the so-called warm Arctic–cold Eurasian (WACE) pattern since it often appears with the warming over the Barents Sea (Overland et al. 2011; Inoue et al. 2012). Along with the appearance of the WACE anomaly pattern, frequent and severe cold events hit East Asian countries during recent years, causing persistent low temperatures and heavy snowfall over Japan in December 2005 and over southern China in January–February 2008 (Honda et al. 2009). The physical cause of increasing Eurasian cold events or the WACE pattern has attracted considerable attention (Honda et al. 2009; Cohen et al. 2012, 2014; Wu et al. 2013; Screen and Simmonds 2013a,b, 2014; Screen et al. 2013, 2014; Sato et al. 2014; Simmonds and Govekar 2014). Many studies have demonstrated that midlatitude Eurasian cold winters are closely tied to the autumn (Honda et al. 2009; Francis et al. 2009; Petoukhov and Semenov 2010; Liu et al. 2012) and winter (Inoue et al. 2012; Tang et al. 2013; Mori et al. 2014) arctic sea ice loss through changes in atmospheric circulations.

The numerical experiments of Newson (1973) first suggested that under an ice-free Arctic Ocean condition, the decrease of the temperature gradient between the equator and pole weakens westerly winds in midlatitudes, which favors atmospheric blocking and thus has consequences for regional temperatures. A suite of sea ice change experiments were conducted by Murray and Simmonds (1995), who also found a reduction in the strength of the westerlies north of about 45°N, albeit with large regional variations in the weakening. This result was also noted in subsequent studies (Liu et al. 2012; Tang et al. 2013; Walsh 2014), while midlatitude cold anomalies are regional. This hints that frequent Eurasian cold events as observed in the recent decade (Zhang et al. 2012) may be related to the arctic warming through a reduction of midlatitude westerly winds (Honda et al. 2009; Petoukhov and Semenov 2010; Inoue et al. 2012; Liu et al. 2012; Tang et al. 2013). Honda et al. (2009) noted that the amplification of the Siberian high as a result of stationary Rossby waves generated thermally by the anomalous turbulent heat fluxes due to the autumn sea ice loss over the Barents and Kara Seas tends to cause colder winters over the Far East. Inoue et al. (2012) found that the northward shift of cyclone tracks under a light ice situation over the Barents Sea creates an anomalous anticyclonic circulation over the Siberian coast, thus generating a warm Arctic–cold Siberian temperature anomaly. However, in a long-term perspective, cold surface air temperature (SAT) anomalies are absent over midlatitude Eurasia, although strong positive SAT anomalies appear over the less ice-covered regions around Greenland and over the Barents Sea (Deser et al. 2000, their Fig. 7).

The numerical experiments of Sato et al. (2014) also indicated that the local response to the heating due to the sea ice loss over the Barents Sea does not produce a midlatitude cold anomaly over Eurasia if the forcing outside the arctic region is not considered. Instead, they concluded that the planetary wave train due to the warming in the Gulf Stream extension region is important for the excitation of the WACE dipole pattern (Sato et al. 2014; Nakanowatari et al. 2014; Simmonds and Govekar 2014). More recently, Dai et al. (2015) also found that during 1999–2013 the DJF cold anomaly over Eurasia is associated with the cold sea surface temperature (SST) anomalies in the central and eastern Pacific possibly as a result of the interdecadal Pacific oscillation (IPO) phase change. Thus, atmospheric teleconnection patterns initiated outside the arctic region may play an important role in the appearance of midlatitude cold anomalies over Eurasia.

Many studies have examined the atmospheric responses to the arctic sea ice loss (Deser et al. 2000; Alexander et al. 2004; Magnusdottir et al. 2004; Deser et al. 2004, 2007; Kvamstø et al. 2004; Seierstad and Bader 2009; Koenigk et al. 2015). Most of these studies showed that the reduction in summer or winter sea ice extent leads to winter atmospheric circulation anomalies resembling the negative phase of the North Atlantic Oscillation (NAO^-) or Arctic Oscillation (AO^-) (Alexander et al. 2004; Magnusdottir et al. 2004; Seierstad and Bader 2009), which is characterized by arctic warming and often leads to midlatitude cold winters (Liu et al. 2012; Tang et al. 2013). Furthermore, Seierstad and Bader (2009) showed that a projected future arctic sea ice reduction for all seasons induces an NAO^--like atmospheric circulation in late winter. However, Deser et al. (2000) found that the reduction of the winter sea ice over the Greenland Sea corresponds to the positive polarity of the NAO and/or AO circulation pattern. Kvamstø et al. (2004) also found that the reduced sea ice extent in the Labrador Sea produces a positive NAO and/or AO response. Thus, it appears that the relationship between the sea ice variations and changes over the arctic region and the phase of the NAO is far from clear. Presumably, the middle-to-high-latitude atmospheric circulation patterns and associated continental cold anomalies depend not only on arctic sea ice variations but also on the forcing outside the

arctic region (Sato et al. 2014; Simmonds and Govekar 2014). This raises an interesting question: Is the recently observed WACE anomaly a direct result of the arctic warming (heating anomaly) over the Barents Sea due to the sea ice loss or a result of the joint influences of the large-scale circulation (NAO and blocking patterns) changes outside the arctic region and the warming over the Barents Sea? As suggested by Walsh (2014) and Francis and Vavrus (2015), the arctic warming tends to favor mid-latitude blocking flows. Thus, it remains an open question whether the WACE pattern is related to an increased frequency (number of days) of Ural blocking (UB) events because the Barents and Kara Seas are influenced by the northern branch of the UB anticyclonic circulation. Such a connection is possible because the blocking anticyclonic anomaly often corresponds to a temperature dipole with a warm anomaly over high latitudes and a cold anomaly over midlatitudes. We investigate this by including and excluding UB events in our observational analysis. Moreover, what processes lead to the increased frequency of UB in the recent decade is also an interesting question. In Part I of this study, we examine these questions with both regression and composite analyses. We also present a new viewpoint that the occurrence of the long-lived UB pattern together with the positive NAO (NAO^+) enhances the WACE temperature anomaly due to the reduction of the westerlies over Eurasia associated with the arctic warming over the Barents Sea. This process may be referred to as the blocking-induced amplification of the reversed meridional temperature gradient that is a manifestation of the WACE dipole pattern. We hypothesize that, although the warming over the Barents Sea does not directly induce the UB pattern, it is a favorable condition for the UB persistence and can strengthen the blocking-induced WACE anomaly pattern. These results differ from previous findings (e.g., Liu et al. 2012; Tang et al. 2013).

This paper is organized as follows: In section 2, we describe the data and methodology. In section 3, the regression and composite analyses are performed to understand the relationship between the WACE pattern and the sea ice loss over the arctic region and its two dominant subregions. The role of UB in the amplification of the WACE pattern is discussed in section 4. In section 5, we examine the impact of decadal variations of surface warming associated with the sea ice loss over the BKS on the UB pattern and its modulation on the WACE pattern. Conclusions and discussion are summarized in section 6.

2. Data and methodology

a. Data

We used daily data of 500-hPa geopotential height and SAT at 2 m on 1° × 1° grids for the winter seasons from December to February (DJF) from ERA-Interim (Dee et al. 2011) from December 1978 to February 2014 (defined as the period 1979–2013 hereafter). Moreover, the monthly SST data on a 0.75° × 0.75° grid were also taken from ERA-Interim. Here we also used the satellite-observed sea ice extent (SIE) monthly data obtained from NSIDC (http://nsidc.org/data/seaice/data_summaries.html) to calculate the spatial pattern of the SIE trend and its time series.

The DJF-mean NAO index was obtained by performing a time average of daily NAO indices during DJF. The daily NAO index is constructed by projecting the daily 500-hPa geopotential height poleward of 20°N onto the loading pattern of the rotated empirical orthogonal functions (REOFs) for the NAO (Barnston and Livezey 1987), from the NOAA/Climate Prediction Center (www.cpc.noaa.gov/products/precip/CWlink/pna/nao.shtml). This index differs slightly from the station-based NAO index defined as the pressure or height difference between the Azores high and the Icelandic low (Hurrell et al. 2003). For the analyses, the daily 500-hPa geopotential height and SAT anomalies are defined as their deviations from the climatological mean for 1979–2013 at each grid point for each day of a winter, and hence the seasonal cycle is removed.

b. Blocking detection method

The UB is a quasi-stationary large-scale anticyclonic circulation occurring around the Ural region that persists for at least one week. To understand the impact of UB on the WACE pattern, we need to identify UB events. The blocking identification method of Tibaldi and Molteni (1990, hereafter TM90), along with its associated TM index, is used to detect such events. The index is defined in terms of 500-hPa geopotential height gradients to the north ($\phi_N = 80°\text{N} + \Delta$) and south ($\phi_S = 40°\text{N} + \Delta$) of a chosen latitude ϕ_0 ($\phi_0 = 60°\text{N} + \Delta$). Here, we use $\Delta = -4°$, 0°, or 4° instead of $\Delta = -5°$, 0°, or 5° in the original TM index because the ERA-Interim data with 1° × 1° grids are used.

On average, blocking events occur in the Ural Mountains region centered at 60°E (Diao et al. 2006), although their center of action can be found as far east as 90°E. A UB event is defined to have taken place when the large-scale conditions specified in TM90 are satisfied and only when the mean position of the positive anomaly averaged over its life cycle is located over the region from 40° to 80°E. The time that a large-scale blocking event satisfies the meridional height gradient condition, $\text{GHGS} = [Z(\phi_0) - Z(\phi_S)]/(\phi_0 - \phi_S) > 0$, of TM90 is defined as its duration, where Z denotes the 500-hPa geopotential height at the specified latitudes. In this paper, our composite analysis is focused on the winters of 1979–2013, and the maximum amplitude of the blocking anticyclonic anomaly during its life cycle is defined as the zero-lag day

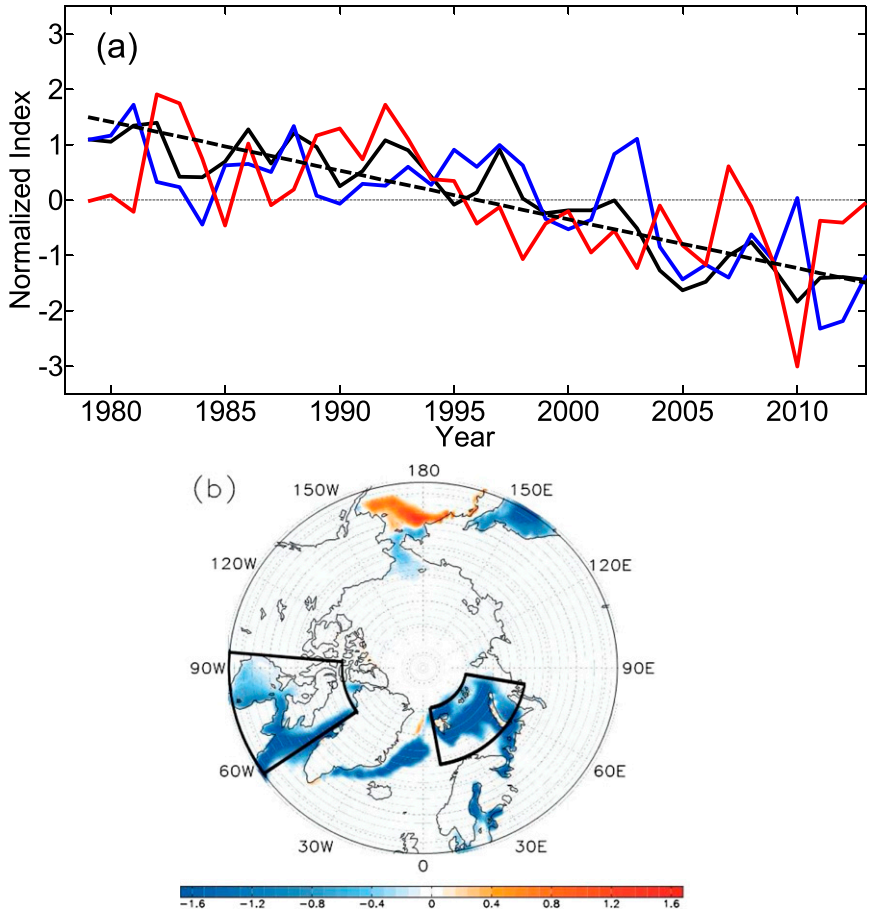

FIG. 1. (a) Time series of normalized 1979–2013 DJF arctic SIE over the whole Arctic (black), BKS (blue), and NAH (red) for nondetrended case, where the dashed line represents the linear trend in the whole-Arctic SIE and (b) the area of the SIE linear trend (% yr^{-1}). The two outlined areas represent the BKS and NAH, respectively.

(lag 0). Moreover, the two-dimensional (2D) blocking index of Davini et al. (2012) is used to examine the change in the center of the UB action from 1979–99 to 2000–13 and the link between the UB and the phase of the NAO by calculating the instantaneous blocking (IB) frequency over Eurasia, which motivates our analysis in Luo et al. (2016, hereafter Part II). Because the frequency distribution of IB events is identical to that of individual blocking events (Davini et al. 2012), only the IB frequency distribution is presented in this paper. For the details of this 2D blocking index and the definition of the IB frequency, refer to the papers of Davini et al. (2012) and Luo et al. (2015).

3. Relationship between the warm Arctic–cold Eurasian anomaly and arctic sea ice loss

a. Atmospheric circulations associated with the winter arctic sea ice loss

To establish the link between arctic sea ice reduction and the winter WACE pattern, it is useful to examine what type of circulation patterns respond to less winter arctic sea ice and to understand where the arctic sea ice loss and associated large-scale circulations play a dominant role in midlatitude cold anomalies over Eurasia. These thoughts lead us to divide the overall arctic sea ice reduction region into two dominant subregions—the BKS and the North American high-latitude (NAH) region (Hudson and Baffin Bay, Davis Strait, and Labrador Sea)—because most of the winter arctic sea ice variability takes place over these two regions. By constructing the SIE time series in the whole arctic region and its two subregions, it is easy to understand where the sea ice loss dominates the whole arctic sea ice reduction by calculating their correlation coefficients. For this, the regressed fields of the 500-hPa geopotential height and surface temperature anomalies onto the SIE time series, for both detrended and nondetrended data, will be presented in this section.

Figure 1a shows the normalized time series of DJF-mean SIE during 1979–2013 over the whole Arctic (solid

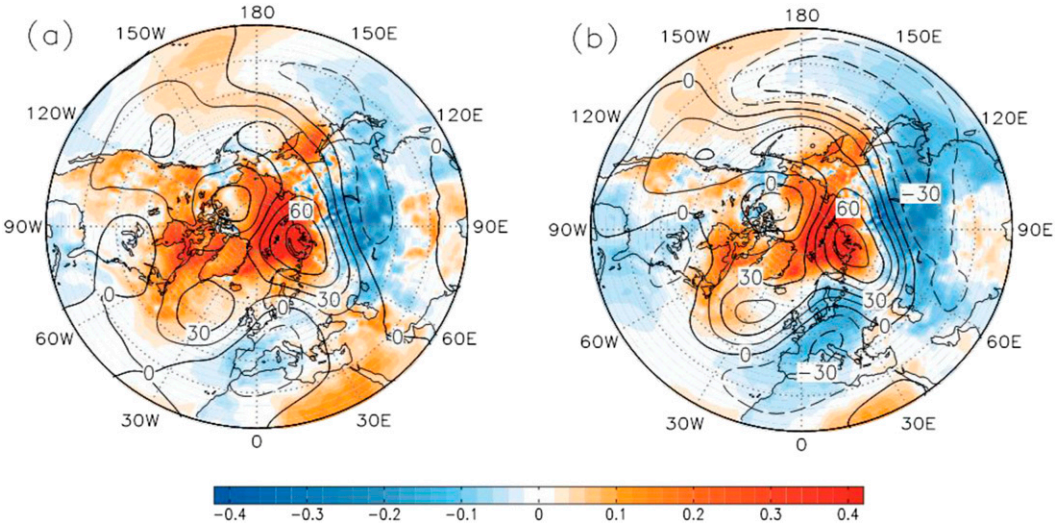

FIG. 2. Linear regression maps of DJF-mean 500-hPa geopotential height [gpm (std dev)$^{-1}$; contour interval = 15 gpm (std dev)$^{-1}$] and SAT [°C (std dev)$^{-1}$; shading] anomaly fields projected onto the SIE time series for (a) nondetrended and (b) detrended cases.

black), the BKS (red), and the NAH (blue). It is seen that winter arctic sea ice has declined steadily from 1979 to 2013, which is statistically significant at the 95% confidence level. The DJF arctic sea ice reduction is overwhelmingly due to declines in the BKS and NAH regions, denoted by the two boxes in Fig. 1b. The SIE time series over the BKS and NAH regions have a positive correlation of 0.78 and 0.62, respectively, with the total arctic SIE, but their correlation coefficients decrease to 0.45 and 0.29 (not significant at the 90% confidence level) after detrending the data. This suggests that on interannual time scales the sea ice variations over the BKS play a bigger role than the NAH sector for the total arctic SIE, consistent with previous findings (Parkinson et al. 1999; Honda et al. 2009). In other words, the loss of sea ice over the BKS dominates the arctic sea ice reduction. If we look at the different atmospheric responses to the sea ice loss in the different sectors, it is feasible to clarify the different role of the sea ice loss in the different regions in midlatitude Eurasian cold anomalies.

The maps of the regression coefficient between local DJF-mean SAT or 500-hPa geopotential height anomaly and the DJF SIE time series (multiplied by −1) are shown in Fig. 2, which shows that accompanying the SIE decreases, the strongest arctic warming occurs over the BKS with strong cooling over the Eurasian continent east of 50°E for the nondetrended (Fig. 2a) and detrended (Fig. 2b) cases, which form a WACE pattern similar to the warm Arctic–cold Siberian pattern as noticed in previous studies (Honda et al. 2009; Inoue et al. 2012). Moreover, a strong warming is also seen in the NAH region and a portion of the North Atlantic (red areas in Fig. 2a) and is related to the sea ice loss in these regions. Accompanying the surface warming, the 500-hPa geopotential height shows positive anomalies around the whole arctic region and weak negative anomalies along the Northern Hemisphere midlatitudes (Fig. 2a). The most prominent characteristic of the Northern Hemisphere circulation is that a strong positive height anomaly emerges near the Ural Mountains (60°E) (contours in Fig. 2a). This large-scale feature can also be seen in Fig. 2b for the detrended case. Although this large-scale anticyclonic circulation is located to the north side of the Ural Mountains, it is still referred to as the UB circulation hereafter, partly because the arctic warming over the BKS changes the UB shape. Moreover, we can see from Fig. 2b that the positive height anomaly over the North Atlantic is stronger and located farther north for the detrended case (Fig. 2b). This demonstrates that the warming trend associated with the arctic sea ice loss weakens the anticyclonic circulation over the North Atlantic and forces it to shift southward. This result is easily explained. This is because the NAO$^+$ pattern corresponds to a negative-over-positive dipole height anomaly over the North Atlantic, and the prevalence of the NAO$^+$ dipole pattern can weaken high-latitude blocking and strengthen midlatitude anticyclonic circulation in the North Atlantic.

On the other hand, because the arctic and subarctic regions over the continental side are mainly covered by the positive height anomalies and the SAT anomaly exhibits a positive-over-negative dipole meridional structure over Eurasia (Fig. 2b), the arctic sea ice loss on interannual time scales is accompanied by an AO$^-$-like pattern and a WACE pattern (Honda et al. 2009;

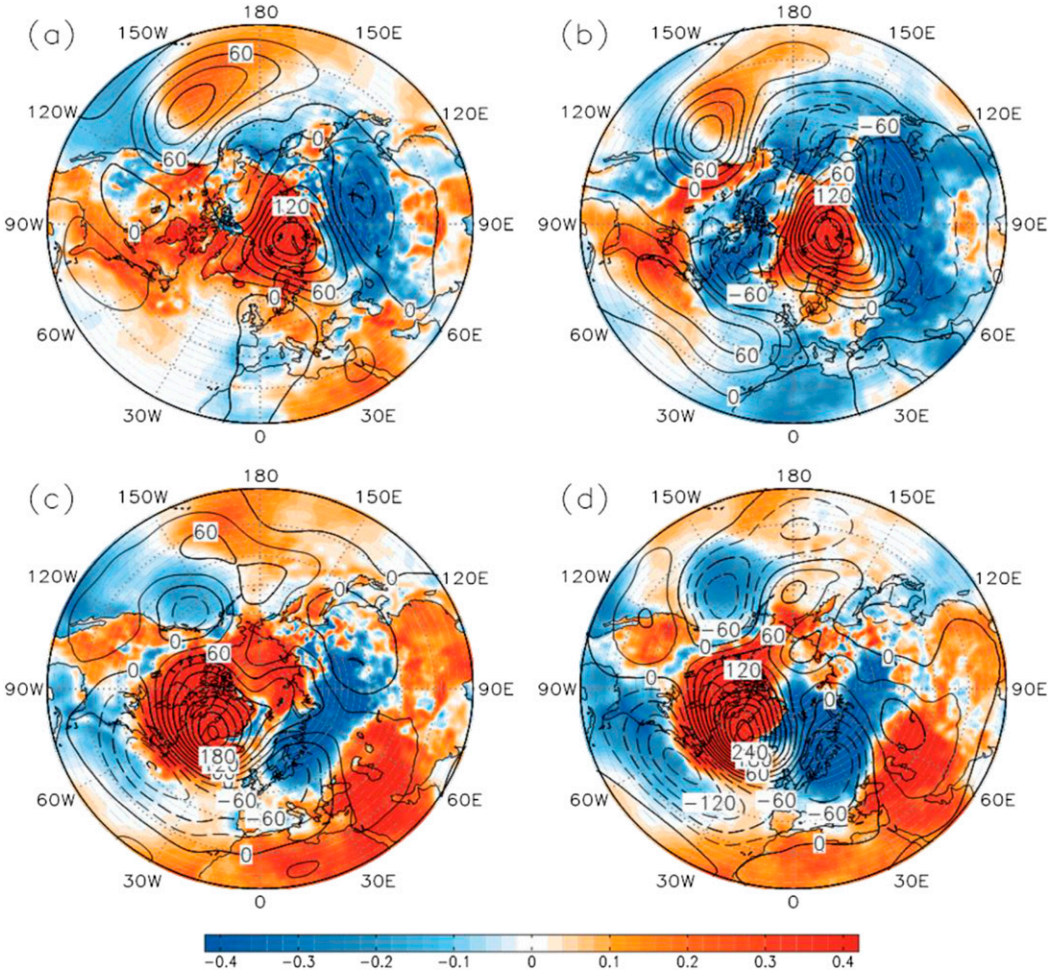

FIG. 3. Linear regression maps of DJF-mean 500-hPa geopotential height [gpm (std dev)$^{-1}$; contour interval = 30 gpm (std dev)$^{-1}$] and SAT [°C (std dev)$^{-1}$; shading] anomaly fields projected onto the SIE time series of the (a),(b) BKS and (c),(d) NAH. Nondetrended case in (a),(c) and detrended case in (b),(d).

Petoukhov and Semenov 2010; Liu et al. 2012; Tang et al. 2013; Vihma 2014; Francis and Vavrus 2015). This suggests that the SIE, SAT, and 500-hPa geopotential height anomalies are physically related. Although a strong UB circulation is seen to occur with the arctic sea ice loss, it is unknown whether the UB anticyclone is related to the sea ice loss over the BKS or the NAH or both. To understand the role of the sea ice loss over different regions, it is useful to present the regressed fields of the 500-hPa geopotential height and SAT anomalies onto the sea ice time series over these two regions.

Figure 3 shows the linear regression maps of the 500-hPa geopotential height and SAT anomalies projected onto the SIE time series (multiplied by −1) over the BKS and NAH. For nondetrended data, the UB anticyclone is dominant around the whole Northern Hemisphere (NH) when the sea ice loss occurs over the BKS (Fig. 3a). However, after detrending, an NAO$^+$-like pattern is seen to coexist with the UB pattern that is especially strong (Fig. 3b). The combined NAO$^+$ and UB anomalies form a teleconnection circulation similar to a negative-phase East Atlantic/West Russia (EA/WR$^-$) pattern (Fig. 3b) according to the definition of Barnston and Livezey (1987). However, the atmospheric circulation pattern associated with the sea ice loss in the NAH region does not exhibit such a structure. In contrast, it resembles an NAO$^-$ pattern with a cold anomaly over high-latitude Eurasia and corresponds to a positive SAT anomaly in the NAH region for both the nondetrended (Fig. 3c) and detrended (Fig. 3d) cases. This differs from the finding of Kvamstø et al. (2004), who noted that the sea ice reduction in the Labrador Sea corresponds to an NAO$^+$ pattern. Thus, the above results indicate that the UB is related to the sea ice loss over the BKS but not to the sea ice loss in the NAH.

As found by Sato et al. (2014) in a numerical model, the Gulf Stream warming can drive a planetary wave

train similar to the EA/WR$^-$ pattern across the Eurasian continent starting from the North Atlantic. The local response to the BKS warming cannot excite such a wave train structure, although it can generate a large-scale anticyclone over the subarctic region and drive a cold anomaly over high-latitude eastern Siberia. This suggests that the UB is not only influenced by the direct forcing of the BKS warming but also by the warming of the mid-latitude North Atlantic (red in Fig. 3b). As further emphasized by Sato et al. (2014), the BKS region may be only an amplifier of the Gulf Stream remote response. This prompts us to consider the combined role of large-scale circulations due to the forcing outside the arctic region and the sea ice loss over the BKS in order to understand the physical cause of the WACE pattern variability. While the sea ice loss over the BKS corresponds to the strong UB together with the NAO$^+$ pattern, the sea ice reduction in the NAH is found to correspond to an NAO$^-$ pattern with a surface warming in the NAH region. Although the large-scale anomaly circulation over the whole Northern Hemisphere associated with the arctic sea ice loss (Fig. 2b) exhibits a positive-over-negative dipole height anomaly around the middle-to-high latitudes with a large positive anomaly in the Eurasian arctic region around the region from the BKS to Ural Mountains, it is different from the AO$^-$ pattern that has a dominant positive anomaly over the North Atlantic and is nearly indistinguishable from the NAO$^-$ pattern (Deser 2000; Feldstein and Franzke 2006). Here we call it a negative Arctic response oscillation (ARO$^-$) pattern. In contrast, it is referred to as a positive ARO (ARO$^+$) pattern when it has an opposite spatial structure (see Fig. 15c). The ARO$^-$ pattern may be understood as comprising the NAO$^-$ pattern related to the sea ice loss over the NAH (Fig. 3d) and the UB pattern associated with the NAO$^+$ pattern (Fig. 3b) related to the sea ice loss over the BKS. This view helps explain, as a response to the overall arctic sea ice loss, why the positive height anomaly over the North Atlantic (Fig. 2b) is shifted to the south of Greenland.

b. *Physical relation of the ARO$^-$ pattern to the arctic sea ice loss and the role of UB*

To understand the role of the local sea ice loss, it is useful to define the DJF-mean SAT anomalies averaged over the regions 60°–85°N, 40°–80°E and 60°–85°N, 90°–50°W as the BKS temperature (BKST) and NAH temperature (NAHT), respectively. The nondetrended and detrended BKST and NAHT time series are shown in Figs. 4a,b together with the arctic SIE. The nondetrended BKST (NAHT) shows a negative correlation of −0.55 (−0.52) with the total arctic SIE, and these correlations strengthen to −0.84 (−0.77) after the application of a five-point moving average. Detrending the data

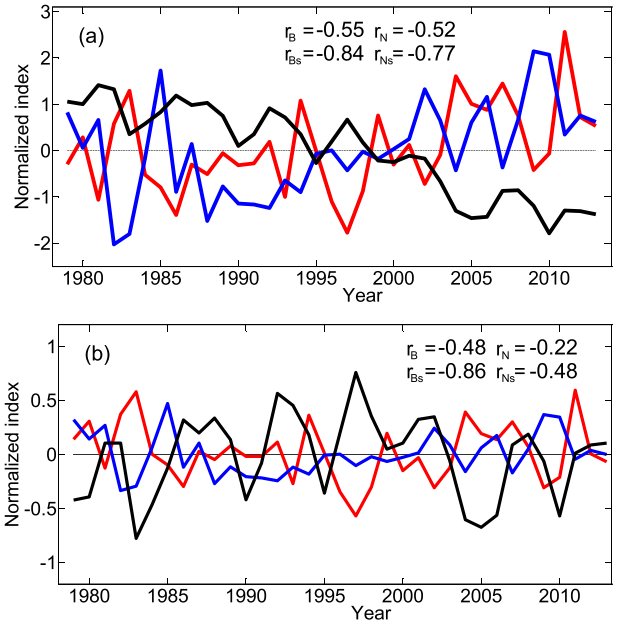

FIG. 4. Time series of (a) nondetrended and (b) detrended DJF-mean SIE (black), BKST (red), and NAHT (blue) indices during 1979–2013, where r_B (r_N) represents the correlation coefficient of the BKST (NAHT) index with the arctic total SIE index and r_{Bs} (r_{Ns}) denotes the correlation coefficient of the same indices after 5-point moving averaging.

reduces the magnitude of the correlation to −0.48 (−0.22), or −0.86 (−0.48) after the smoothing. Thus, arctic total SIE decreases are more closely related to the warming over the BKS than over the NAH (Honda et al. 2009; Petoukhov and Semenov 2010). In this case, the surface air warming over the BKS or NAH may be identified as corresponding to the sea ice loss over each sector.

Because the nondetrended SAT anomalies over the BKS and NAH regions are mostly positive after 2000 (Fig. 4a), it is also insightful to split 1979–2013 into two epochs: P1 (1979–99) and P2 (2000–13). Such a period split is reasonable for examining the decadal variations of the SAT anomaly, although the warming in the North Atlantic during 1979–2013 is associated with the AMO (Peings and Magnusdottir 2014) and the SST related to the IPO phase change (Dai 2013; Dong and Dai 2015), and the inflow of North Atlantic warm waters into the BKS occurred after 2000 (Spielhagen et al. 2011; Alexeev et al. 2013; Walsh 2014).

It is also helpful to perform the linear regressions of the 500-hPa geopotential height and SAT anomalies onto the arctic SIE time series (multiplied by −1) during P1 and P2 (Figs. 5a–d) for both detrended and nondetrended cases. This can help us better understand the variation of atmospheric circulation patterns associated with the winter sea ice loss from P1 to P2. It is seen that although there is a strong positive height anomaly over

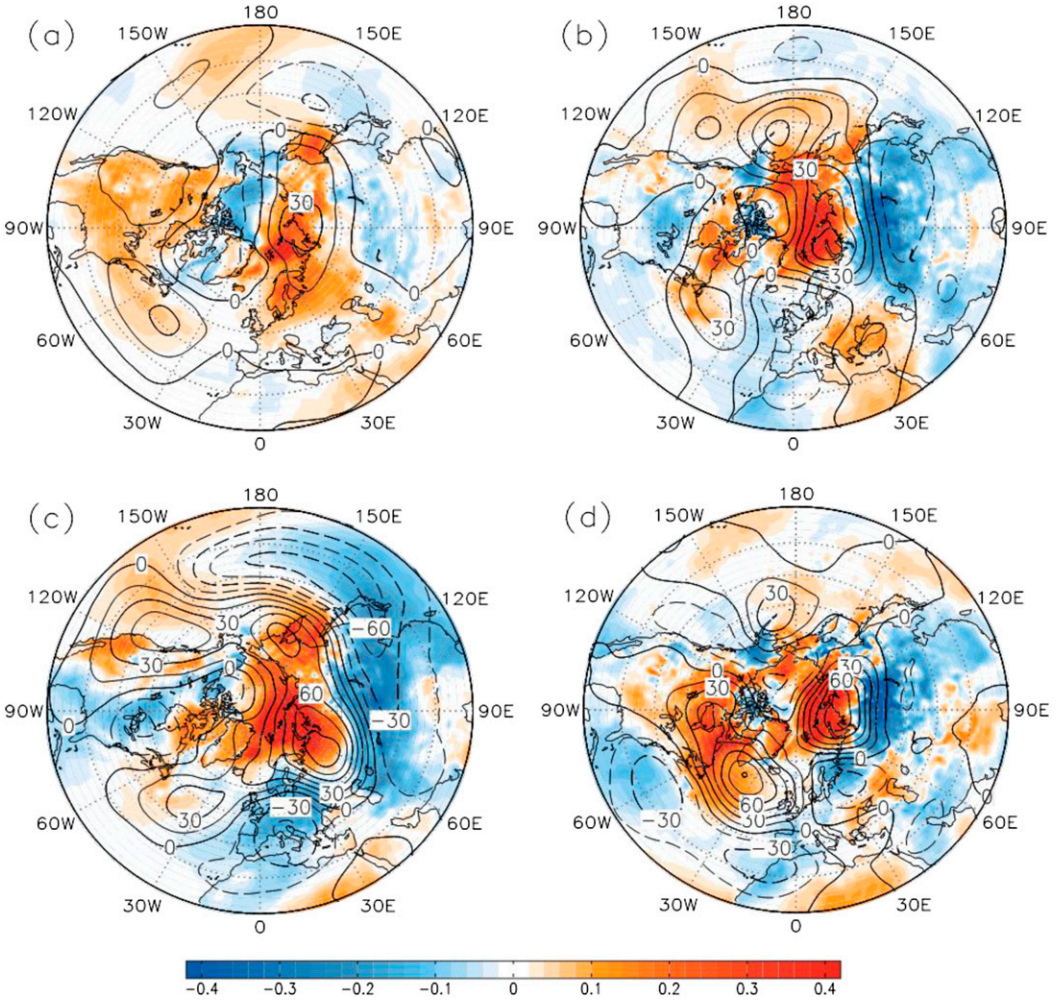

FIG. 5. Linear regression maps of DJF-mean 500-hPa geopotential height [gpm (std dev)$^{-1}$; contour interval = 15 gpm (std dev)$^{-1}$] and SAT [°C (std dev)$^{-1}$; shading] anomaly fields projected onto the arctic SIE time series during (a),(c) P1 and (b),(d) P2 for the case with trends in (a),(b) and without trends in (c),(d).

central Siberia near the Ural Mountains during P1 and P2 (Figs. 5a,b), this anticyclonic anomaly is stronger for P2 than for P1. The strongest surface warming takes place over the BKS, while a cold anomaly appears over Eurasia (Figs. 5a–d). When the data are detrended, we can see that blocking anticyclones still exist over two regions: southern Greenland and the Ural Mountains and the northeastern side of the Ural Mountains (Figs. 5c,d). An important difference of this is that over the North Atlantic the blocking anticyclone is stronger and located over the southern tip of Greenland during P2, while it is weaker and located in the midlatitude North Atlantic during P1. In particular, during P2 the North Atlantic blocking is not identical to the Greenland blocking associated with the NAH sea ice loss (Figs. 3c, d). This reflects that during P2 other circulation patterns not related to the NAH sea ice variability may change the location and strength of the North Atlantic blocking. Moreover, the UB tends to occur in the higher-latitude region during P2. This suggests that the atmospheric response to arctic sea ice loss is complex. It could be argued that it depends not only on the regional specifics of arctic warming but also on the atmospheric circulation patterns related to the forcing outside the arctic region (Sato et al. 2014; Simmonds and Govekar 2014).

Why does the Northern Hemisphere circulation exhibit such an ARO^{-}-like pattern? We conclude that it is likely a synthesis of the atmospheric circulation patterns related to the sea ice reduction over the NAH and BKS regions. This can be verified by calculating the regression fields of 500-hPa geopotential height and SAT anomalies onto the BKST and NAHT time series, respectively. Figure 6 shows the regressed patterns of the detrended 500-hPa geopotential height anomaly against

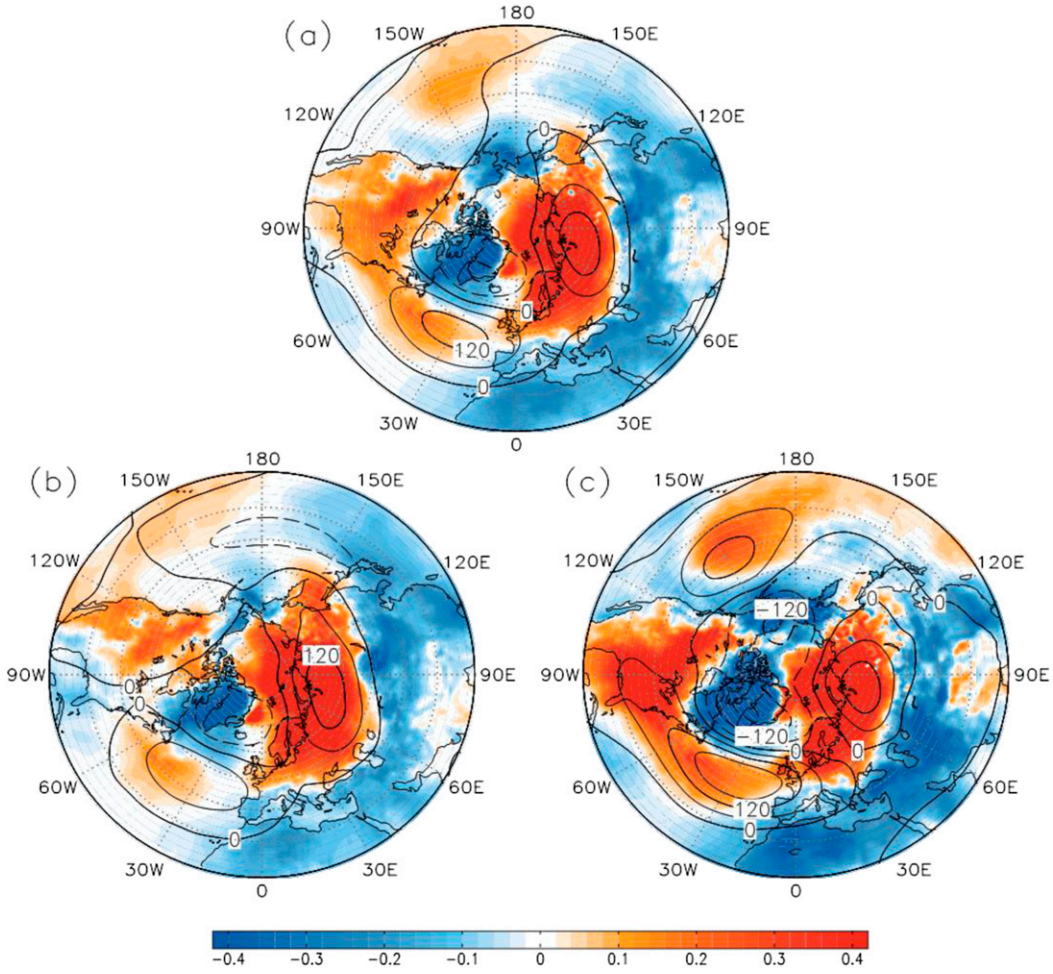

FIG. 6. Linear regression maps of detrended DJF-mean 500-hPa geopotential height [gpm (std dev)$^{-1}$; contour interval = 60 gpm (std dev)$^{-1}$] and SAT [°C (std dev)$^{-1}$; shading] anomaly fields projected onto the detrended BKST index shown in Fig. 4 during (a) 1979–2013 and its two epochs, (b) P1 and (c) P2.

the detrended BKST time series during 1979–2013 and its two epochs P1 and P2. We find that the regressed height field shows an NAO$^+$-like dipole in the North Atlantic and an UB anticyclone near the Ural Mountains. In other words, the large-scale circulation associated with the BKS warming exhibits a planetary wave train that is comprised of the NAO$^+$ pattern and UB anticyclone. This wave train structure exists during P1 and P2 although its intensity is changed from P1 to P2 (Figs. 6b,c). Correspondingly, the SAT anomaly shows a warming over the subarctic region and a cooling over the midlatitude Eurasian continent, a WACE dipole temperature anomaly. However, the numerical experiment of Sato et al. (2014) indicated that the BKS warming cannot directly excite the NAO$^+$ pattern. It is possible that the NAO$^+$ pattern contributing to the WACE pattern comes from the midlatitude North Atlantic warming. As we note in Part II, the sea surface warming over midlatitude North Atlantic occurs together with the oceanic warming over the BKS. While the midlatitude North Atlantic warming favors the NAO$^+$ pattern (Czaja and Frankignoul 2002), the oceanic warming over the BKS favors the sea ice loss there and then reduces the middle-to-high-latitude westerly winds over Eurasia to produce a favorable condition that increases the persistence of UB events. The regressed fields of 500-hPa geopotential height and SAT anomalies onto the NAHT time series for 1979–2013 and its two epochs P1 and P2 also show that when the warming takes place over the NAH region, the height anomaly exhibits an NAO$^-$ pattern during 1979–2013 and P1, but it resembles a Greenland blocking anticyclone during P2 (not shown). Naturally, the ARO$^-$-like pattern related to the sea ice loss over the whole Arctic during P2 may be explained as a superimposition of the NAO$^-$ pattern and the UB anticyclone together with the NAO$^+$ pattern

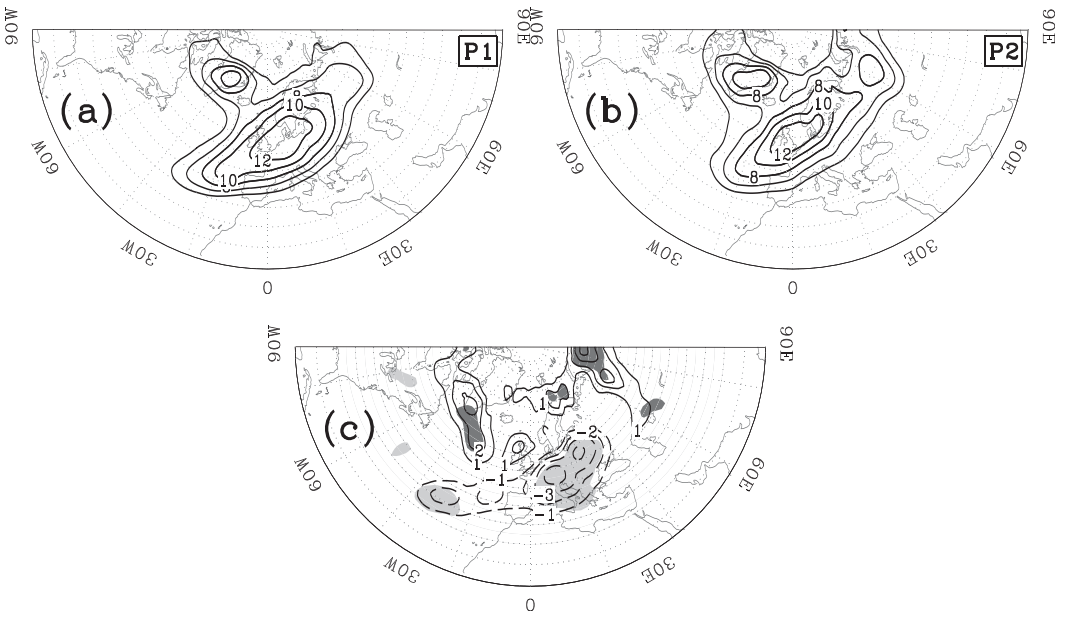

FIG. 7. Horizontal distribution of winter-mean instantaneous blocking frequency (%) during (a) P1 and (b) P2, and (c) the P2 − P1 difference. The shading denotes the region above the 95% confidence level using a two-sided Student's *t* test.

related to the warming over the NAH, BKS, and midlatitude North Atlantic (Figs. 3 and 6). Such a superimposition in the North Atlantic can make the anticyclonic anomaly center of the North Atlantic blocking shift southward during P2. However, as noted above, the AO^- pattern has a dominant North Atlantic component and is identical to the NAO^- pattern (Deser 2000; Feldstein and Franzke 2006). Thus, it is difficult to explain the WACE pattern using the AO^- pattern (or equivalent NAO^- pattern) because the NAO^- pattern does not correspond to a WACE temperature anomaly. But for the ARO^--like pattern as seen from Fig. 2, the UB is actually a very important component that constructs the main body of the ARO^--like pattern (Fig. 5d). Thus, it becomes feasible to explain the WACE pattern with the ARO^- viewpoint if the ARO^--like pattern can be explained as a superimposition of the NAO^- pattern related to the NAH sea ice loss and the strong UB anticyclone together with the NAO^+ pattern associated with both the BKS sea ice loss and midlatitude North Atlantic warming. In the following section, we will emphasize and quantify the role of the UB in the WACE variability.

4. Role of Ural blocking in the warm Arctic–cold Eurasian pattern amplification

Because the regression analysis cannot tell us how the lifetime of UB events changes from P1 to P2, it is necessary to identify the individual UB events in winter during 1979–2013 and calculate their life periods in terms of the blocking indices. Here, we first use the 2D index of Davini et al. (2012) to determine the spatial distribution of the UB frequency and its variation from P1 to P2. Then, the TM index is utilized to calculate the life period of each UB event.

Before picking UB events, it is of value to look at the IB frequency distribution in winter during 1979–2013. Figure 7 shows the winter (DJF) spatial distribution of IB frequency (the percentage of IB days with respect to the total days of a winter) for the P1 and P2 periods. It is seen that there is a higher IB frequency over the Ural region during P2 (Fig. 7b) than during P1 (Fig. 7a). In addition, the P2 − P1 difference (Fig. 7c) shows that the higher IB frequency tends to take place in the higher-latitude region from Greenland to the Ural region. Because the high IB frequency corresponds to more blocking days, it is not surprising that high IB frequencies are found in the region of long-lived blocking events. In particular, the increase in the IB frequency over the south of the BKS and the north of the Ural Mountains is distinct (Fig. 7c), indicating that the warming over the BKS due to arctic sea ice loss increases the persistence of the UB anticyclone, especially its northern branch. Although the UB is long lived during P2, its intensity is slightly less than during P1 (see Figs. 14c,d). As shown below, the strong warming due to the sea ice loss over the BKS during P2 tends to reduce the middle-to-high-latitude westerly wind over Eurasia, thus providing a background condition favoring long-lived UB events.

We identify 54 UB events over the Ural region (40°–75°N, 40°–80°E) during 1979–2013. In these events,

31 (1.48 yr^{-1}, with a total number of 235 days) occurred during P1 and 23 (1.64 yr^{-1}, with a total number of 194 days) occurred in P2. While the yearly number of the UB events has increased by about 11% from P1 to P2, the yearly blocked days have increased by 24% from 11.2 days per winter during P1 to 13.9 days per winter during P2, with the mean lifetime increasing from 7.6 to 8.4 days. This indicates that the frequency (number of days) of UB events has increased from P1 to P2 largely because of its prolonged lifetime for the individual UB event. The mean number of days with the IB events for each winter is 18 (22) days during P1 (P2).

a. The statistical relationship between the UB, NAO, and BKS warming

To further reveal the link between the UB and WACE patterns, it is necessary to establish a statistical relationship between the UB, NAO, and BKS warming. Before examining this problem, we should first discuss the time-mean fields of the 500-hPa geopotential height and SAT anomalies during the UB life cycle with a quasi-biweekly time scale (10–20 days) averaged from lag −10 to +10 days (where lag 0 denotes the UB peak) during 1979–2013. Figure 8a shows the time-mean 500-hPa geopotential height and associated SAT anomaly fields for all the UB events averaged over 20 days centered on the UB peak day. It is seen that when the UB occurs, the SAT exhibits a typical quasi-biweekly WACE (QB-WACE) anomaly, in which the surface warming or positive SAT anomaly emerges on the northern side of the UB anticyclonic anomaly center with a cold anomaly on its southeastern side. This hints that the emergence of the QB-WACE anomaly is linked to the presence of UB events. If this QB-WACE anomaly event is long lived, the strong DJF-mean WACE anomaly will emerge over Eurasia. For this case, the further loss of the BKS sea ice is enhanced in a wider area. At the same time, we can see in Fig. 8a that there is an anticyclonic anomaly over the midlatitude North Atlantic. It reflects that the North Atlantic large-scale circulation can be projected into the NAO^+ pattern while it is relatively weak and its negative component is not present over Greenland. This can be explained as follows: In Fig. 8a the time mean of 500-hPa geopotential height anomalies develops around the UB peak (lag 0). Naturally, it is inevitable that the time-mean NAO^+ pattern averaged over the life cycle of the UB is weak because there is an approximate 4–7-day time lag of the UB behind the NAO^+, as we will see in Part II. In Fig. 8b we construct the time series of the normalized DJF-mean UB frequency (days with UB), BKST index, and NAO index, based upon the result in Fig. 8a. It is seen that the BKST index exhibits an

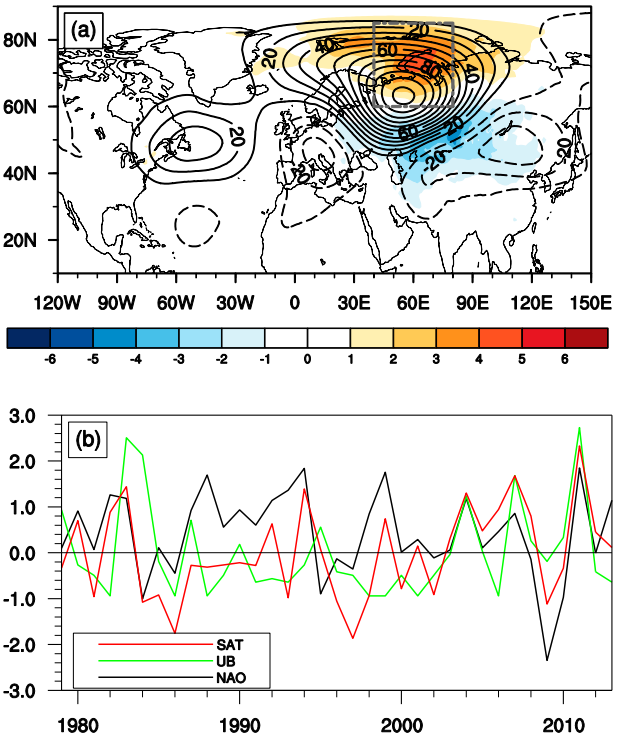

FIG. 8. (a) Time-mean 500-hPa geopotential height (gpm; contour interval = 10 gpm) and SAT (K; color shading) anomalies averaged from lag −10 to 10 days. (b) Time series of normalized DJF-mean NAO (black) and SAT (red) averaged over the region 60°–85°N, 40°–80°E and UB frequency (green) indices during 1979–2013. In (a), lag 0 denotes the day of the UB peak and the dashed box denotes the BKS.

upward trend from 1979 to 2013 but shows almost no trend during P1, whereas a significant upward trend is seen during P2. During P2 the upward trend of the BKST index concurs with the increasing UB frequency that is stronger during P2 than during P1 (Fig. 8b).

Further correlation analyses show that during 1979–2013 the BKST index exhibits a positive correlation of 0.45 (0.57) with the UB frequency (NAO) index, while the UB frequency has negligible correlation (0.02) with the NAO index. This at least reflects that the warming over the BKS is related to the increased UB frequency and the NAO^+ phase. The correlation between the UB and NAO indices changes from −0.31 during P1 to 0.45 during P2, while the positive correlation of the BKST and UB frequency (NAO) indices increases from 0.20 to 0.72 (from 0.64 to 0.77) from P1 to P2. For detrended data, similar results are found (not shown). In particular, the correlation coefficient between the UB frequency and NAO index becomes 0.51 (significant at the 90% confidence level) during P2. The strong positive correlation between any two of the three indices during P2 is easily explained. Because the midlatitude North Atlantic warming is more intense during P2 than during P1

(Fig. 16a in Part II), NAO^+ events are more easily excited during P2 as a response (Czaja and Frankignoul 2002). The theoretical result of Luo et al. (2007) indicates that the decay of the NAO^+ event can frequently excite downstream blocking. The resultant downstream blocking tends to occur in the Ural region and be long lived because of the reduced westerly winds over the Ural Mountains and its adjacent region induced by the BKS warming (see Fig. 11b). In this case, it is inevitable that there is a strong positive correlation between the NAO index and UB frequency during P2. As further shown in Fig. 8a, the occurrence of the UB pattern can induce an additional warming over the BKS (dashed box in Fig. 8a) on time scales of 10–20 days and amplify the warming over the BKS prior to the UB onset (see Fig. 15b) to establish an intense DJF-mean WACE pattern (see Fig. 15d). Such an interaction is the so-called positive feedback between the UB and DJF-mean WACE patterns. Naturally, the BKST index exhibits a strong positive correlation with the UB frequency during P2. Because the NAO^+ pattern corresponds to an increased UB frequency (see Fig. 16a), there is an enhanced positive correlation between two of the BKST, UB, and NAO indices during P2. However, how the phase of the NAO and its variability affects the UB and associated WACE variability is explored in Part II of this study.

b. *UB-induced amplification of the WACE pattern*

Here, we define $DT = \Delta T_S - \Delta T_N$ as an intensity index for characterizing the variations of the winter-mean WACE pattern, where ΔT_N and ΔT_S denote the regional-mean SAT anomalies over the arctic region (60°–85°N, 40°–80°E) and the Eurasian continent (40°–60°N, 50°–90°E), respectively. If DT is strongly negative, then the WACE pattern is strong. Otherwise, the WACE pattern is weak. Figure 9a shows that the DJF-mean DT index and UB frequency are highly correlated (the correlation coefficient is −0.70 during 1979–2013). It is noteworthy that this correlation becomes stronger during both subperiods, with −0.80 in P1 and −0.93 in P2; that is to say, the high UB frequency corresponds to a strong reversed meridional temperature gradient in winter. Thus, the WACE pattern is a manifestation of the UB frequency. Associated with the increasing UB frequency during P2, the WACE pattern is intensified (Fig. 9a). Consequently, the intensified WACE patterns with intense cold Eurasian midlatitude winters in the recent decade are likely related to the increased UB frequency associated with the sea ice loss over the BKS during P2 winters.

To see whether the BKS warming contributes to the UB and if the WACE pattern is related to the quasi-stationary wave train from the North Atlantic to Eurasia (Honda et al. 2009; Sato et al. 2014), it is useful to examine the difference of the winter-mean 500-hPa geopotential height anomalies between strong and weak WACE patterns. Here we define the strong (weak) WACE pattern as the case with the DJF-mean DT index equal to or less (greater) than −0.5 (0.5) standard deviations. We then computed the difference of the DJF-mean 500-hPa geopotential height and SAT anomaly between the strong and weak WACE patterns (Fig. 9b). It is clear that the height anomaly difference exhibits a negative-over-positive dipole anomaly in the North Atlantic (NAO^+ pattern) and a reversed dipole anomaly over the Ural region (UB pattern). By definition, a warm-over-cold SAT dipole temperature anomaly like a WACE pattern is seen over Eurasia as well. Thus, the WACE pattern appears together with the NAO^+ and concurrent UB patterns; that is, the combined NAO^+ and downstream UB patterns exhibit a planetary wave train structure. This is the likely cause of why there is a positive correlation of the NAO index with the UB frequency and BKST indices during P2 as seen from Fig. 8b.

However, it is difficult to identify the causal relationship between the BKS warming and UB pattern because they are coupled together. An efficient method to reveal causality is to calculate the DJF-mean WACE indices with and without blocking events and then examine their difference. We show the time series of DJF-mean WACE index for two cases with and without blocking events in Fig. 10. It is seen that the WACE index is mostly negative during 2000–13, especially after 2004. The WACE index becomes more negative once the blocking events are involved (solid line in Fig. 10). Obviously, the presence of the UB pattern can amplify the WACE pattern through strengthening the reversed SAT meridional gradient over Eurasia. The difference of the WACE index between the two cases with and without blocking further shows that the UB-induced DJF-mean warming does not remember the decadal signal of the sea ice loss (warming) over the BKS because the UB-induced WACE index does not show a downward trend during P2 (red line in Fig. 10). It is possible that the decadal variation of the warming over the BKS or the WACE pattern likely comes from oceanic processes such as the inflow of Atlantic warm water into the arctic region, AMO, and SST anomalies during P2 (Walsh 2014; Peings and Magnusdottir 2014), even though the UB can amplify the BKS warming.

5. The modulation of the decadal UB and warming variations on the WACE pattern

a. *Background conditions of long-lived UB events*

In the above sections, although we have quantified the UB-induced amplification role of the winter-mean WACE

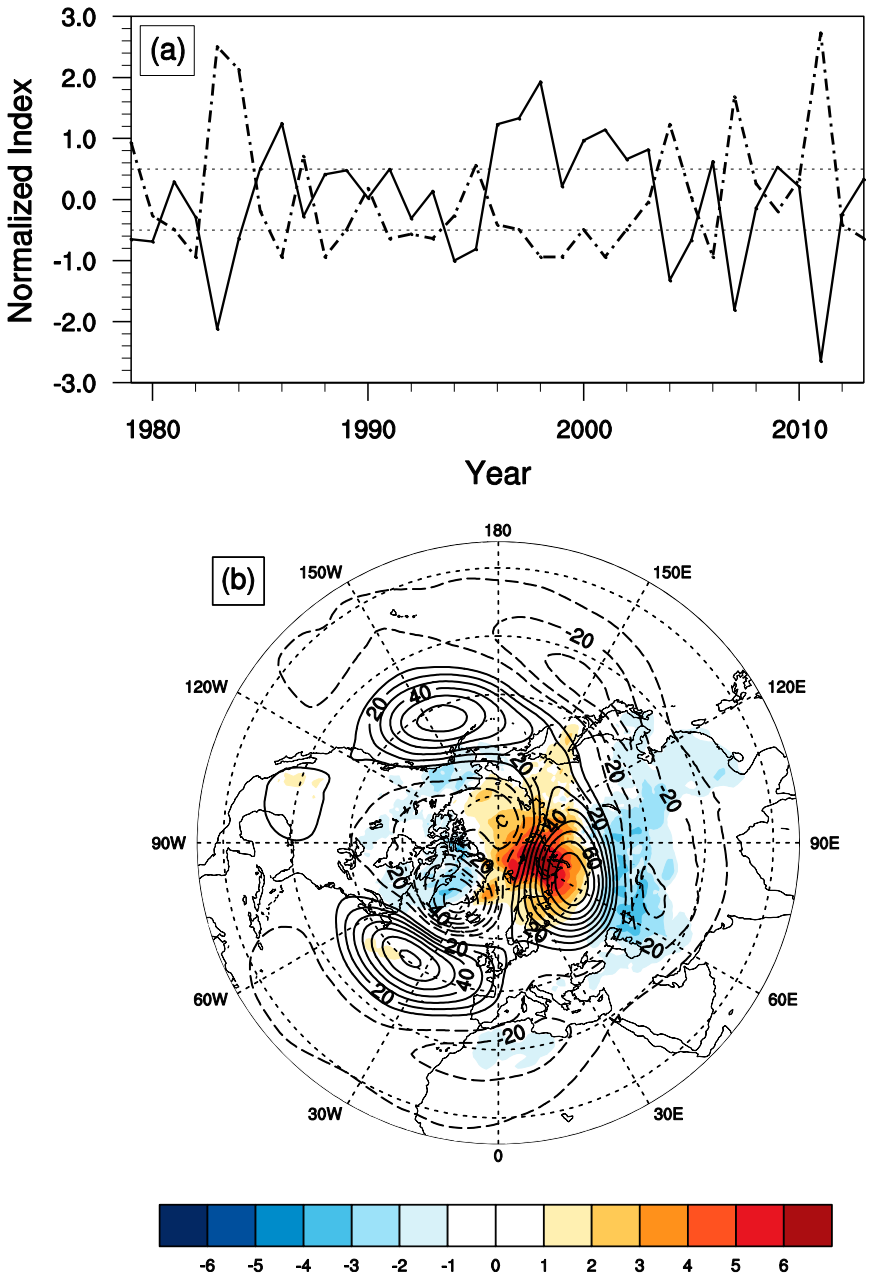

FIG. 9. (a) Time series of normalized DJF-mean WACE index DT (solid) and UB frequency (dashed). (b) The differences of the DJF-mean 500-hPa geopotential height (gpm) and SAT (K) anomalies between the strong (DT ≤ -0.5°C) and weak (DT ≥ 0.5°C) WACE cases.

pattern, the roles of the decadal UB and warming variations in changes in the spatial structure of the WACE pattern are not sufficiently understood. Before investigating this problem, it is useful to explore the decadal variation of UB from P1 to P2 and what background conditions favor long-lived UB events during P2 in this subsection.

To understand why the UB events are longer lived during P2, it is useful to look at the background westerly wind change from P1 to P2. To quantify the background westerly wind, we need to exclude daily zonal winds associated with UB events to calculate the winter-mean background westerly wind. We show the DJF-mean westerly wind averaged during P1 and its difference with P2 (P2 minus P1) in Figs. 11a,b and the time series of normalized DJF-mean westerly wind strength averaged over the region 50°–70°N, 50°–80°E (mean westerly wind strength hereafter) during 1979–2013 in Fig. 11c. It is found that during P1 the middle-to-high-latitude

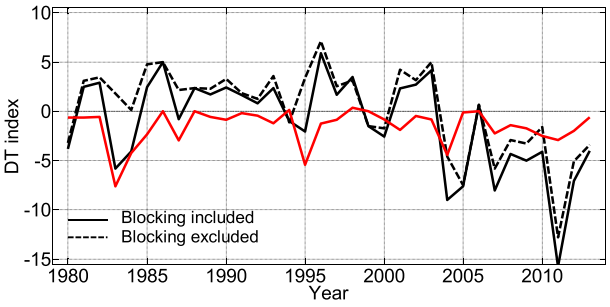

FIG. 10. Time series of the DJF-mean WACE indices DT (°C) with (solid black) and without (dashed black) the effect of Ural blocking and their difference (red).

westerly winds are weaker over Eurasia than over the Atlantic basin (Fig. 11a). This result is also detected for P2 (not shown). The P2 − P1 difference clearly shows that the DJF-mean westerly wind strength along the middle-to-high-latitude region from the North Atlantic to Eurasia is weaker during P2 than during P1 (Fig. 11b). While this westerly wind reduction (~30%) from P1 to P2 is seen along the latitudes from 50° to 70°N over Eurasia, the percentage decrease of the westerly wind over Eurasia is larger than over the North Atlantic. Figure 11c also shows that there is a negative correlation of −0.54 (statistically significant at the 95% confidence level) between the mean westerly wind strength and UB frequency during P2. This indicates that during P2 the reduced middle-to-high-latitude westerly wind due to the BKS warming is a favorable condition for the persistence of UB events, thus explaining why the UB has a higher frequency during P2 in Fig. 7. Although Newson (1973) also mentioned this point, much more information about where the westerly wind is weakened and how the UB and BKS warming interact was not provided in his study.

b. *Roles of decadal UB events and surface air temperature in the WACE pattern variability*

To examine the impact of the UB event variation from P1 to P2 on the WACE pattern, it is reasonable to calculate the time-mean (composite) 500-hPa geopotential height and SAT anomaly fields averaged over the life cycles of individual UB events during P1 and P2 and their P2 − P1 difference. As shown in Fig. 8b, over the BKS the warming trend actually reflects the decadal variation of the SAT anomaly. Thus, the detrending of the height and temperature fields corresponds essentially to the removal of the decadal variations of these fields. If the data are detrended, the decadal SAT variations due to the arctic sea ice loss will be removed. Here we performed additional analyses based on the detrended and nondetrended cases. For the two cases we show the time-mean 500-hPa geopotential height and

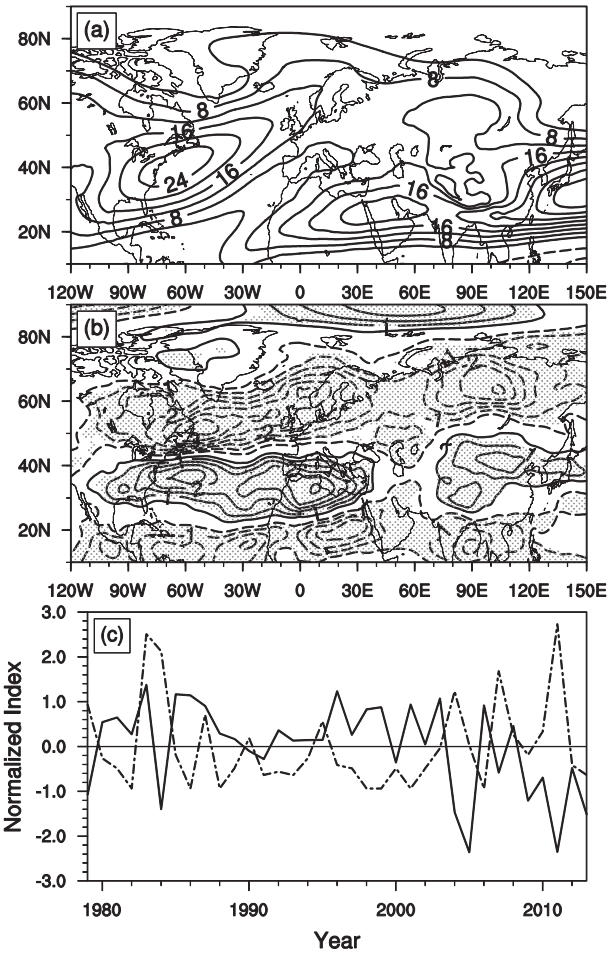

FIG. 11. (a) DJF-mean zonal wind (m s^{-1}) with blocking events excluded during P1 and (b) the P2 − P1 difference (m s^{-1}; contour interval = 1.0 m s^{-1}). (c) Time series of normalized DJF-mean zonal wind strength with blocking events excluded (solid) and UB frequency during 1979–2013 (dashed). In (b), the shading denotes the region above the 95% confidence level.

SAT anomaly fields averaged over the UB life cycle for two epochs P1 and P2 and their difference in Figs. 12a–f. It is seen that when the raw data are used, there are more intense and widespread UB anticyclonic circulations during P2 (Fig. 12b) than during P1 (Fig. 12a). Similarly, the high-latitude warming is more pronounced and widespread for P2 (shading in Fig. 12b) than for P1 (shading in Fig. 12a), which is readily apparent in the P2 − P1 SAT difference field (Fig. 12c). The positive SAT anomaly over the BKS in the P2 − P1 SAT difference field (Fig. 12c) reflects the intense decadal surface warming due to the BKS sea ice loss during P2.

The P2 − P1 500-hPa geopotential height difference field (Fig. 12c) also shows that a planetary wave train originating from the midlatitude North Atlantic propagates into the Barents Sea region during P2 relative to

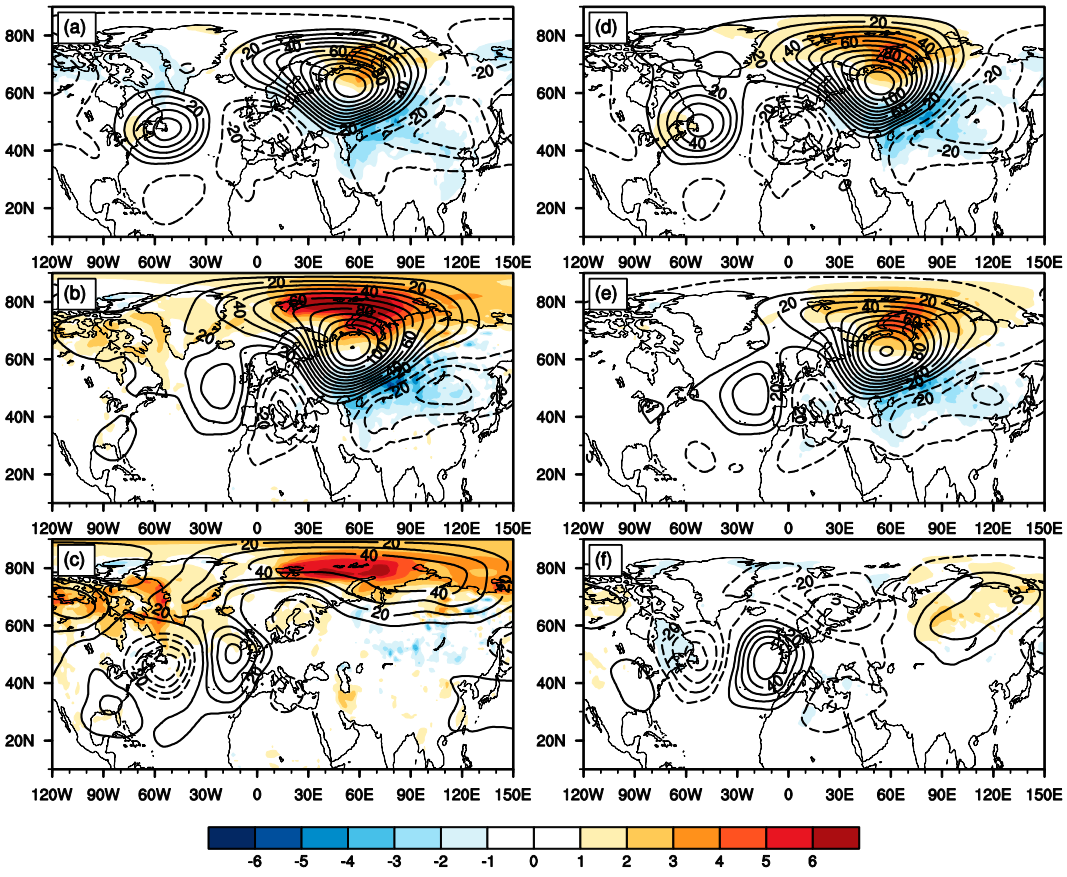

FIG. 12. Time-mean (a)–(c) nondetrended and (d)–(f) detrended 500-hPa geopotential height (gpm) and SAT (K; shading) anomalies averaged during the blocking life period from lag −10 to 10 days for (a),(d) P1 and (b),(e) P2 and (c),(f) their difference, where lag 0 denotes the blocking peak.

P1 and then strengthens and enlarges the blocking anticyclone in the subarctic side. For the detrended time-mean 500-hPa geopotential height and SAT anomaly fields (Figs. 12d–f), the wave train structure is still visible in the P2 − P1 500-hPa geopotential height difference field (Fig. 12f), but its anticyclonic anomaly becomes evidently weak and tends to be located in central-east Siberia. For this case, the BKS warming almost disappears. Thus, during P2 the positive SAT anomaly over the BKS and associated WACE pattern are essentially a manifestation of the decadal SAT variation and UB-induced warming. On the other hand, we see that the center of the UB action is slightly located more northward for the nondetrended case (Fig. 12b) than for the detrended case (Fig. 12e). Although the change in the location of the UB anticyclonic anomaly center from P1 to P2 is less evident, the northern branch of the UB anticyclone is remarkably intensified and widened because of the sea ice loss over the BKS during P2 (Fig. 12b). The intense and wide UB can induce a stronger dipole temperature anomaly during P2 (Fig. 12b) than during P1 (Fig. 12a) to produce an intense WACE pattern because the UB is long lived and its frequency undergoes an upward trend during P2.

c. *Evolutions of daily UB and SAT anomalies*

It is also important to examine the daily fields of composite UB and SAT anomalies to reveal how the UB patterns evolve during P1 and P2. We show the composite detrended daily 500-hPa geopotential height and SAT anomaly fields during P1 and P2 in Fig. 13. It is seen that during P1 there is a positive height anomaly over the midlatitude western North Atlantic and a weak negative height anomaly over Greenland during the UB life cycle (Fig. 13a). This dipole anomaly looks like an NAO^+ pattern. In this NAO^+ pattern a positive anomaly is seen to be located in the midlatitude North Atlantic near the Gulf Stream region (Sato et al. 2014). The decay of this NAO^+ pattern is so weak that we cannot conclude that the UB results from the wave train propagation or the energy dispersion of the NAO^+

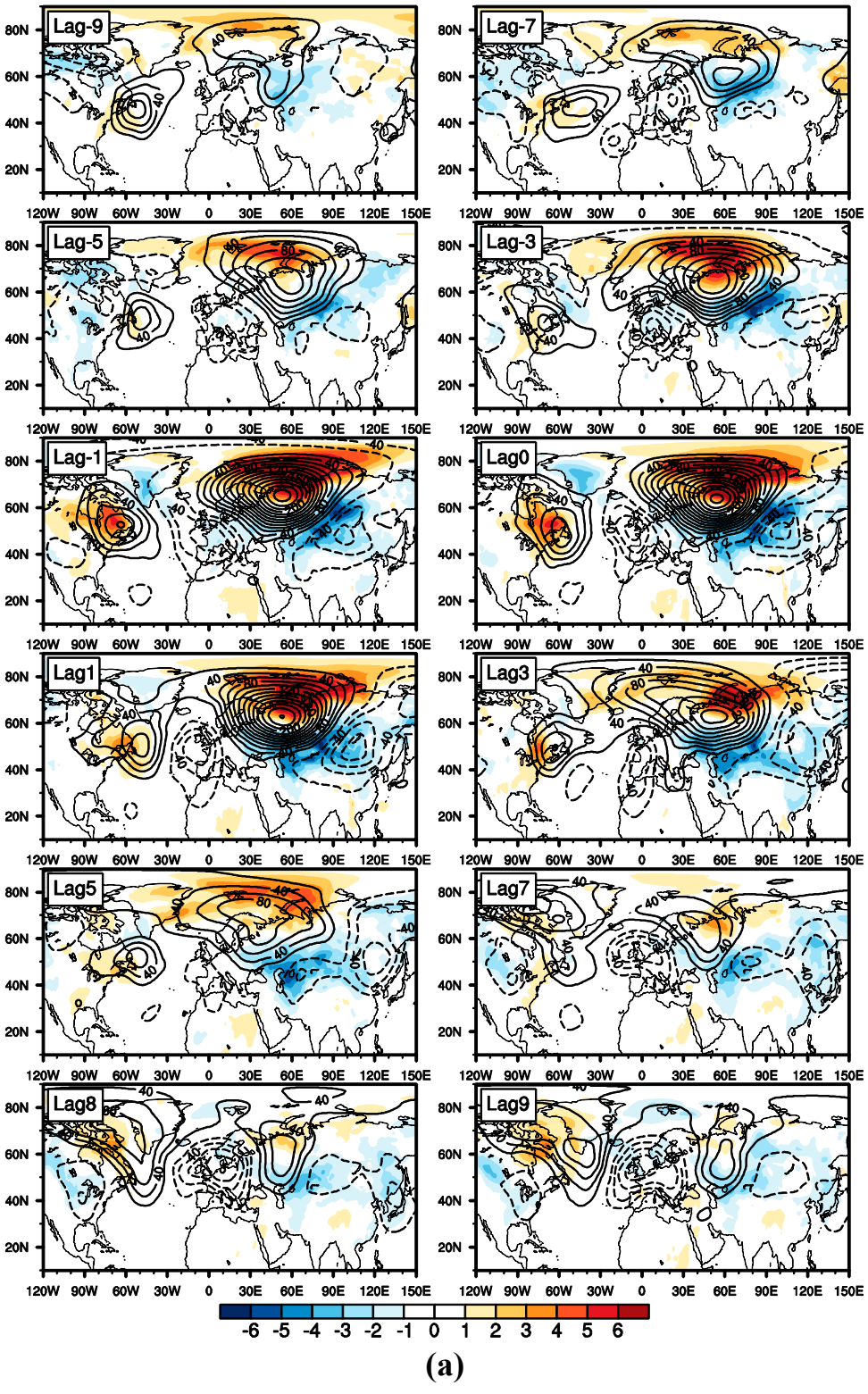

FIG. 13. Instantaneous fields of composite detrended daily 500-hPa geopotential height (gpm; contour interval = 10 gpm) and SAT (K; color shading) anomalies during the period from lag −9 to 9 days during (a) P1 and (b) P2, where lag 0 denotes the peak of the UB amplitude.

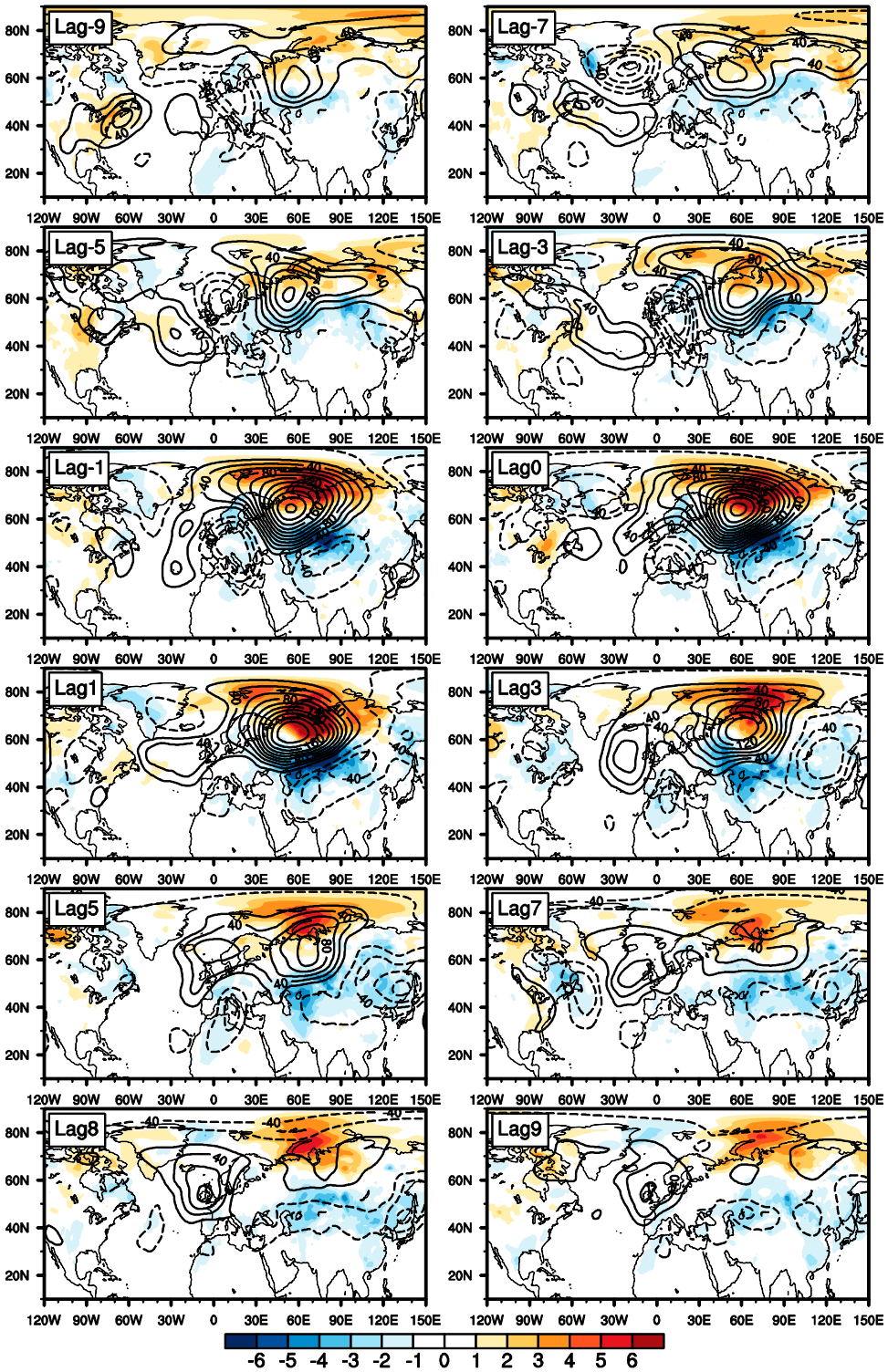

(b)

FIG. 13. (*Continued*)

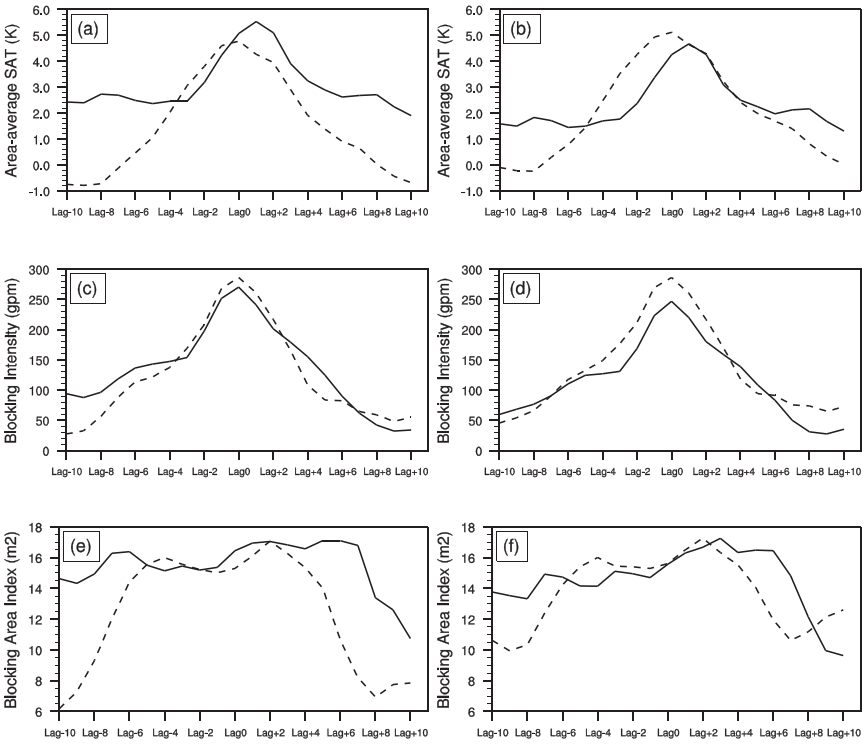

FIG. 14. Time evolution of area-averaged, composite daily (a),(b) SAT, (c),(d) blocking intensity, and (e),(f) B_σ (m^2) with the positive anomaly ≥10 gpm during the UB life cycle from lag −10 to 10 days for nondetrended cases in (a),(c),(e) and detrended cases in (b),(d),(f), in which the solid (dashed) line represents the case of P2 (P1), and lag 0 denotes the day that the UB anticyclone peaks.

pattern (Fig. 13a). For this case, the UB may be unrelated to the NAO^+ pattern during P1, thus explaining why there is a lower correlation between the DJF-mean NAO index and UB frequency during P1. However, this feature is not present during P2 (Fig. 13b). An NAO^+ pattern appears at lag −7 days. Accompanying its persistent decay from lag −7 to lag 0 day, a planetary wave train is seen in the North Atlantic and the Eurasian continent as well as a UB pattern being formed over the Ural region. Thus, it is concluded that during P2 the UB occurrence is more likely related to the energy dispersion or planetary wave train propagation resulting from the decay of the NAO^+ pattern. This problem is examined in detail in Part II. Although the UB anticyclone is weaker after lag 7 days for P2 than for P1, it is stronger before lag −7 days. In this case, an important result is found that during P2 the UB establishment is a slow process, while the UB decay is rapid. The cause of the asymmetry of the UB growth and decay deserves further exploration but is beyond the scope of this study. Moreover, the detrended daily WACE anomaly is more persistent during P2 (Fig. 13b) than during P1 (Fig. 13a). This is more evident for a nondetrended case (not shown). The likely cause of this result is that the composite UB anticyclone during P2 has a relatively large area to transport more warm air to the arctic region to lead to a long-lasting warming over the BKS or a long-lived QB-WACE anomaly. This point can be further seen from composites of the daily 500-hPa geopotential height and SAT fields for UB events below.

To quantify the variation of the UB and associated SAT anomalies, we define the value of the maximum positive anomaly center of the UB as the UB intensity. The blocking area B_σ is defined as the area over which height anomalies exceed 10 gpm. Similar to the definition in section 3, we define the SAT anomaly averaged over the domain 60°–85°N, 40°–80°E as the UB-induced area-average SAT anomaly.

We show the time evolution of the composite daily area-average temperature, blocking intensity, and blocking area from lag −10 to 10 days in Fig. 14. It is interesting to see that the UB-induced arctic warming is more intense and persistent during P2 than during P1 (solid line in Fig. 14a). Although the UB is weaker during P2 than during P1, it has a larger area (Figs. 14e,f) and is more persistent (Figs. 14c,d) during P2 for the detrended and nondetrended cases. During P2 the wide and persistent blocking circulation transports more

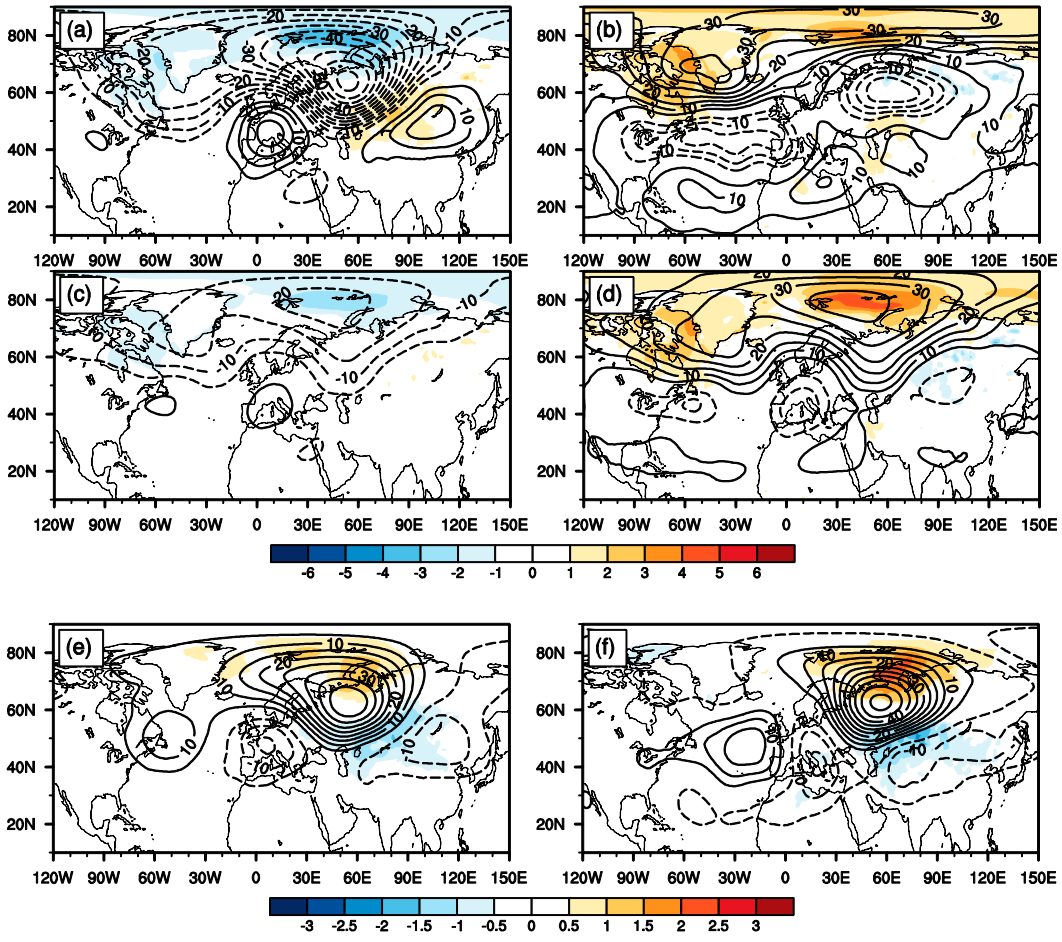

FIG. 15. DJF-mean 500-hPa geopotential height (gpm; contour interval = 10 gpm) and SAT (K; color shading) anomalies (relative to the 1979–2013 mean) (a),(b) without blocking events (i.e., the time interval from lag −10 to lag +10 days of a UB was excluded, where lag 0 denotes the blocking peak) and (c),(d) with blocking events during (a),(c) P1 and (b),(d) P2. The winter-mean difference between two cases is shown for UB events included and excluded during (e) P1 and (f) P2.

warm air to the arctic region around the BKS, thus producing a long-lasting arctic warming (Figs. 14a,b). In particular, the SAT anomaly becomes more persistent and its largest intensity lags the UB peak by 1 day owing to the BKS sea ice loss. On the other hand, we see from Figs. 14c,d that the UB establishment is a slow process, but its decay is a rapid process. This is consistent with the result obtained from the composite daily height anomaly in Fig. 13. Because the UB establishment is slower, it can accumulate more heat over the BKS region so that a large positive SAT anomaly can still be seen over the BKS even when the UB decays rapidly. This explains why the QB-WACE anomaly can be persistently maintained during P2 (Fig. 13b). Thus, during P2 the decadal SAT variation due to the BKS sea ice loss can make the UB-induced QB-WACE anomaly more persistent. Based on these results, it is concluded that in the recent decade the joint role of the UB-induced QB-WACE anomaly and arctic warming over the BKS tends to make Eurasian cold winters more persistent and intense. However, it is difficult to learn from the above results how the spatial structure of the winter-mean WACE pattern changes from P1 to P2. This problem will be examined in the next subsection.

d. The role of UB in the change in the spatial structure of the winter-mean WACE pattern

We show the DJF-mean 500-hPa geopotential height and SAT anomalies during P1 and P2 in Figs. 15a,b (Figs. 15c,d) for UB events excluded (included). Figure 15f (Fig. 15e) shows the Fig. 15d minus Fig. 15b (Fig. 15c minus Fig. 15a) difference of the DJF-mean 500-hPa geopotential height and SAT anomalies between the two cases with and without blocking events for P2 (P1). We see that there are anticyclonic anomalies over both the BKS and Greenland when the UB events are excluded

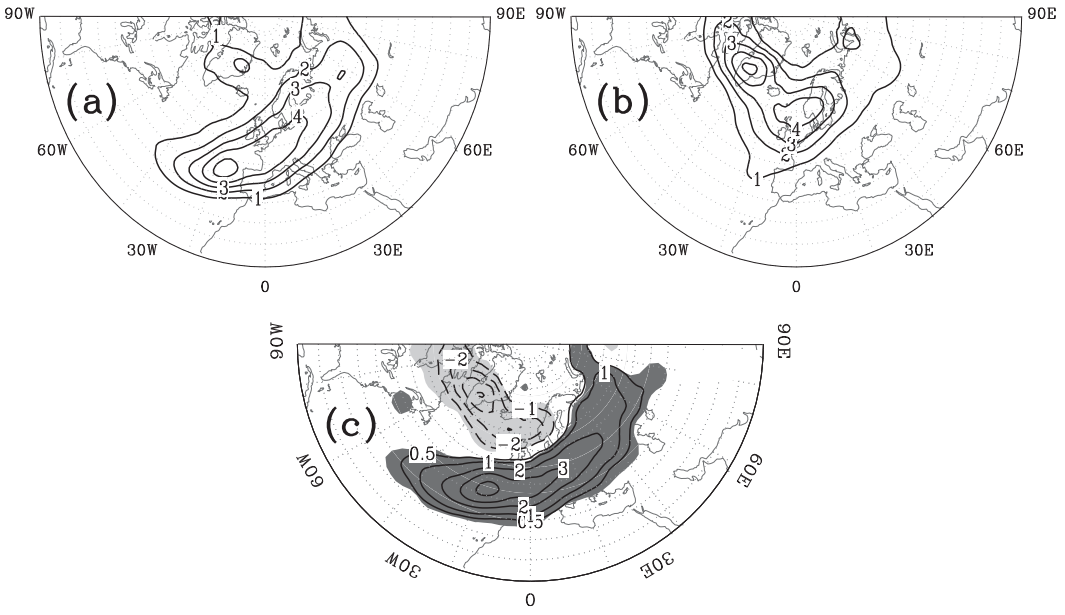

FIG. 16. Horizontal distributions of the IB frequency (%) associated with (a) NAO^+ and (b) NAO^- events during their life cycles (from lag −10 to lag +10 days, where lag 0 denotes the NAO peak) and (c) their frequency difference [(a) minus (b)], in which the shading denotes the region above the 95% confidence level for a two-sided Student's *t* test.

(contours in Fig. 15b). A negative height anomaly is also seen in the south of the BKS region. The cold SAT anomaly is seen in the high latitudes between 60° and 70°N, while a warm STA anomaly emerges over the BKS (color in Fig. 15b). However, we can further see that when the UB events are included, the anticyclonic anomaly is intensified over the BKS and its anticyclonic area is widened, but weakened over Greenland, as shown in the winter-mean height anomaly field (contours in Fig. 15d). This means that the DJF-mean height anomaly shows an east–west seesaw between the BKS and Greenland, reflecting that the emergence of the UB events is more likely related to the NAO^+ pattern (contours in Fig. 15f). Because of the role of the UB pattern (Fig. 15f), the BKS warming-induced DJF-mean anticyclonic anomaly is intensified and widened and then expands toward the south (Fig. 15d), consistent with the regressed results (Figs. 2b and 3b). In addition, the surface air warming over the BKS is also intensified and widened to establish an intense WACE pattern (color in Fig. 15d). This reflects the joint role of UB- and BKS-warming-induced SAT anomalies. That is to say, the UB-induced SAT anomalies can amplify the WACE temperature anomaly to form an intense DJF-mean WACE pattern. The cold anomaly of the WACE pattern is seen to shift southward so that it is located south of 60°N because of the presence of UB (color in Fig. 15d). Thus, the presence of the UB pattern can cause the cold anomaly of the WACE pattern to shift toward the midlatitudes to affect midlatitude countries. It is further found that while the detrended UB height anomaly averaged from lag −10 to lag +10 days is weaker in P2 (Fig. 12e) than in P1 (Figs. 12d), the DJF-mean UB anomaly is stronger during P2 (contour in Fig. 15f) than during P1 (contour in Fig. 15e) because the UB is more persistent during P2. It is also seen that the UB-induced DJF-mean WACE pattern is more intense for P2 than for P1. In particular, the DJF-mean cold anomaly is more intense and located in lower latitudes during P2 (color in Fig. 15f) than during P1 (color in Fig. 15e). Thus, it is concluded that intense winter cold events in midlatitude Eurasian continents will increase if the sea ice loss over the BKS continues and the UB is present.

e. *Is the UB related to the NAO?*

As suggested by Fig. 15f, the UB anomaly is related to the upstream NAO^+ pattern. To establish this point, we show the frequency distribution of IB events associated with the life cycles (from lag −10 to 10 day, lag 0 denotes the NAO peak) of NAO^+ and NAO^- events during 1979–2013 in Fig. 16 according to the NAO definition that the daily NAO index must attain one standard deviation (1.0 STD) for at least three consecutive days, as described in Part II. It is obvious that the UB frequency (number of days) is higher for the NAO^+ phase (Fig. 16a) than for the NAO^- phase (Fig. 16b), thus indicating that the UB is long lived for the NAO^+ phase. Their difference is statistically significant at the 95% confidence level (Fig. 16c). This result also holds for a 0.5-STD definition (not shown). This suggests that the

variation of the NAO outside the arctic region is also important for the variability of the WACE pattern via the UB change. Thus, it is necessary to examine the impact of the NAO variability on the UB to reveal the physical cause of the winter WACE variation. This is reported in Part II.

6. Conclusions and discussion

In this paper, we have examined the impact of Ural blocking on the warm Arctic–cold Eurasian (WACE) temperature pattern in winter (DJF) by dividing the arctic sea ice loss region into two main subregions: the Barents and Kara Seas and North American high-latitude regions. The regressed maps of 500-hPa geopotential height and SAT anomalies onto the winter SIE time series show that there are blocking anticyclones over the North Atlantic and the Ural region resembling an ARO^- pattern. This ARO^- pattern is different from the AO^- that has a dominant positive height anomaly over the North Atlantic. In this ARO^--like pattern, the UB pattern is a very important component. Moreover, positive SAT anomalies are also seen over the BKS and NAH regions, respectively. The regression analysis in the different region also shows that for detrended data, the sea ice loss over the BKS corresponds to the UB and concurrent NAO^+ and is followed by a WACE pattern, while the sea ice loss over the NAH region corresponds to an NAO^--like pattern with a cold anomaly over northern Eurasia. These results are new, which can also be seen in the SAT regression field even for the nondetrended data.

Moreover, it is found that the SAT anomaly over the BKS exhibits a distinct positive trend during 2000–13, which reflects a marked decadal variation of the warming over the BKS due to the sea ice loss. By separating 1979–2013 into two epochs, 1979–99 (P1) and 2000–13 (P2), we have found that UB events become more persistent as a result of the reduced middle-to-high-latitude westerly wind (Fig. 11b) induced by the warming (sea ice loss) over the BKS during P2 than during P1. In particular, because of the role of the BKS warming, the UB persistence becomes asymmetric with respect to its peak during P2, in which the establishment of the UB is a slow process and its decay is a relatively rapid process. The slow-growing UB can accumulate more heat over the BKS to maintain a persistent warming, while it is affected by the persistence of the UB. The presence of the long-lived UB event can induce an additional warming over the BKS (dashed box in Fig. 8a) through the emergence of a persistent QB-WACE anomaly event and amplifies the warming over the BKS prior to the UB onset to establish a strong DJF-mean WACE pattern, which leads to further loss of arctic sea ice over the BKS. This is the so-called positive feedback between the UB and WACE patterns. It is also demonstrated that the BKS warming-induced DJF-mean anticyclonic anomaly becomes stronger and wider and then expands toward the south because of the presence of UB during P2. Along with the strengthening and expansion of the anticyclonic anomaly over the BKS, in a DJF-mean field the Eurasian cold anomaly is seen to shift toward midlatitudes (Fig. 15d). This implies that under the condition of the stronger winter sea ice loss over the BKS the midlatitude cold events will be more frequent over the Eurasian continent, while the UB is an important amplifier of the WACE pattern.

On the other hand, we see that the warming over the BKS exhibits a positive correlation with the NAO index and the UB frequency during P2. This can be explained by the close relation between the NAO and UB (Figs. 16a,b) and the close relationship of the BKS warming with the UB (Fig. 8a). The cause of this NAO–UB relation is easily explained using the theoretical result of Luo et al. (2007) based on a nonlinear multiscale interaction model of NAO events, who noted that the decay of the NAO^+ event can lead to downstream blocking through the energy dispersion of Rossby waves. This process can be seen in Fig. 13b. Although our emphasis is placed on examining the impact of the UB on the WACE pattern, the variation of the UB frequency is shown to depend on the phase of the NAO. This motivates us to examine how the variations of the UB and associated QB-WACE anomalies depend on the phase of the NAO and North Atlantic conditions to reveal the physical cause of the WACE variability via the QB-WACE change. Results from that investigation are presented in Part II.

Acknowledgments. The first three authors acknowledge the support from the National Science Foundation of China (Grants 41375067, 41430533, and 41505075). This study was motivated when the first author was a visiting scientist at the State University of New York at Albany during May 2015. A. Dai is supported by the U.S. National Science Foundation (Grant AGS-1353740), the U.S. Department of Energy's Office of Science (Award DE-SC0012602), and the U.S. National Oceanic and Atmospheric Administration (Award NA15OAR4310086). I. Simmonds was supported by Australian Research Council Grant DP 160101997. C. Franzke was supported by the German Research Foundation (DFG) through the cluster of excellence CliSAP. The authors thank three anonymous reviewers and Prof. Walsh, whose comments improved this paper.

REFERENCES

Alexander, M. A., U. S. Bhatt, J. E. Walsh, M. S. Timlin, J. S. Miller, and J. D. Scott, 2004: The atmospheric response to realistic

arctic sea ice anomalies in an AGCM during winter. *J. Climate*, **17**, 890–905, doi:10.1175/1520-0442(2004)017<0890:TARTRA>2.0.CO;2.

Alexeev, V. A., V. V. Ivanov, R. Kwok, and L. H. Smedsrud, 2013: North Atlantic warming and declining volume of arctic sea ice. *Cryosphere Discuss.*, **7**, 245–265, doi:10.5194/tcd-7-245-2013.

Barnston, A. G., and R. E. Livezey, 1987: Classification, seasonability and persistence of low-frequency atmospheric circulation patterns. *Mon. Wea. Rev.*, **115**, 1083–1126, doi:10.1175/1520-0493(1987)115<1083:CSAPOL>2.0.CO;2.

Cohen, J., J. C. Furtado, M. A. Barlow, V. A. Alexeev, and J. E. Cherry, 2012: Arctic warming, increasing snow cover and widespread boreal winter cooling. *Environ. Res. Lett.*, **7**, 014007, doi:10.1088/1748-9326/7/1/014007.

——, and Coauthors, 2014: Recent arctic amplification and extreme mid-latitude weather. *Nat. Geosci.*, **7**, 627–637, doi:10.1038/ngeo2234.

Comiso, J. C., C. L. Parkinson, R. Gersten, and L. Stock, 2008: Accelerated decline in the arctic sea ice cover. *Geophys. Res. Lett.*, **35**, L01703, doi:10.1029/2007GL031972.

Czaja, A., and C. Frankignoul, 2002: Observed impact of Atlantic SST anomalies on the North Atlantic Oscillation. *J. Climate*, **15**, 606–623, doi:10.1175/1520-0442(2002)015<0606:OIOASA>2.0.CO;2.

Dai, A., 2013: The influence of the inter-decadal Pacific Oscillation on U.S. precipitation during 1923–2010. *Climate Dyn.*, **41**, 633–646, doi:10.1007/s00382-012-1446-5.

——, J. C. Fyfe, S.-P. Xie, and X. Dai, 2015: Decadal modulation of global-mean temperature by internal climate variability. *Nat. Climate Change*, **5**, 555–559, doi:10.1038/nclimate2605.

Davini, P., C. Cagnazzo, S. Gualdi, and A. Navarra, 2012: Bidimensional diagnostics, variability, and trends of Northern Hemisphere blocking. *J. Climate*, **25**, 6496–6509, doi:10.1175/JCLI-D-12-00032.1.

Dee, D. P., and Coauthors, 2011: The ERA-Interim reanalysis: Configuration and performance of the data assimilation system. *Quart. J. Roy. Meteor. Soc.*, **137**, 553–597, doi:10.1002/qj.828.

Deser, C., 2000: On the teleconnectivity of the ''Arctic Oscillation.'' *Geophys. Res. Lett.*, **27**, 779–782, doi:10.1029/1999GL010945.

——, J. E. Walsh, and M. S. Timlin, 2000: Arctic sea ice variability in the context of recent atmospheric circulation trends. *J. Climate*, **13**, 617–633, doi:10.1175/1520-0442(2000)013<0617:ASIVIT>2.0.CO;2.

——, G. Magnusdottir, R. Saravanan, and A. Philips, 2004: The effects of North Atlantic SST and sea ice anomalies on the winter circulation in CCM3. Part II: Direct and indirect components of the response. *J. Climate*, **17**, 2160–2176, doi:10.1175/1520-0442(2004)017<0877:TEONAS>2.0.CO;2.

——, R. A. Tomas, and S. Peng, 2007: The transient atmospheric circulation response to North Atlantic SST and sea ice anomalies. *J. Climate*, **20**, 4751–4767, doi:10.1175/JCLI4278.1.

Diao, Y., J. Li, and D. Luo, 2006: A new blocking index and its application: Blocking action in the Northern Hemisphere. *J. Climate*, **19**, 4819–4839, doi:10.1175/JCLI3886.1.

Dong, B., and A. Dai, 2015: The influence of the interdecadal Pacific oscillation on temperature and precipitation over the globe. *Climate Dyn.*, **45**, 2667–2681, doi:10.1007/s00382-015-2500-x.

Feldstein, S. B., and C. Franzke, 2006: Are the North Atlantic Oscillation and the northern annular mode distinguishable? *J. Atmos. Sci.*, **63**, 2915–2930, doi:10.1175/JAS3798.1.

Francis, J. A., and E. Hunter, 2006: New insight into the disappearing arctic sea ice. *Eos, Trans. Amer. Geophys. Union*, **87**, 509–511, doi:10.1029/2006EO460001.

——, and S. J. Vavrus, 2015: Evidence for a wavier jet stream in response to rapid arctic warming. *Environ. Res. Lett.*, **10**, 014005, doi:10.1088/1748-9326/10/1/014005.

——, E. Hunter, J. R. Key, and X. Wang, 2005: Clues to variability in arctic minimum sea ice extent. *Geophys. Res. Lett.*, **32**, L21501, doi:10.1029/2005GL024376.

——, W. Chan, D. J. Leathers, J. R. Miller, and D. E. Veron, 2009: Winter Northern Hemisphere weather patterns remember summer arctic sea-ice extent. *Geophys. Res. Lett.*, **36**, L07503, doi:10.1029/2009GL037274.

Honda, M., J. Inoue, and S. Yamane, 2009: Influence of low arctic sea-ice minima on anomalously cold Eurasian winters. *Geophys. Res. Lett.*, **36**, L08707, doi:10.1029/2008GL037079.

Hurrell, J. W., Y. Kushnir, and G. Ottersen, 2003: An overview of the North Atlantic Oscillation. *The North Atlantic Oscillation: Climatic Significance and Environmental Impact*, *Geophys. Monogr.*, Vol. 134, Amer. Geophys. Union, 1–35, doi:10.1029/134GM01.

Inoue, J., M. E. Hori, and K. Takaya, 2012: The role of Barents Sea ice in the wintertime cyclone track and emergence of a warm-arctic cold-Siberian anomaly. *J. Climate*, **25**, 2561–2568, doi:10.1175/JCLI-D-11-00449.1.

Koenigk, T., M. Caian, G. Nikulin, and S. Schimanke, 2015: Regional arctic sea ice variations as predictor for winter climate conditions. *Climate Dyn.*, **46**, 317–337, doi:10.1007/s00382-015-2586-1.

Kvamstø, N. G., P. Skeil, and D. B. Stephenson, 2004: Impact of Labrador sea-ice extent on the North Atlantic Oscillation. *Int. J. Climatol.*, **24**, 603–612, doi:10.1002/joc.1015.

Kwok, R., G. F. Cunningham, M. Wensnahan, I. Rigor, H. J. Zwally, and D. Yi, 2009: Thinning and volume loss of the Arctic Ocean sea ice cover: 2003–2008. *J. Geophys. Res.*, **114**, C07005, doi:10.1029/2009JC005312.

Liu, J., J. A. Curry, H. Wang, M. Song, and R. M. Horton, 2012: Impact of declining arctic sea ice on winter snowfall. *Proc. Natl. Acad. Sci. USA*, **109**, 4074–4079, doi:10.1073/pnas.1114910109.

Luo, D., A. Lupo, and H. Wan, 2007: Dynamics of eddy-driven low-frequency dipole modes. Part I: A simple model of North Atlantic Oscillations. *J. Atmos. Sci.*, **64**, 3–38, doi:10.1175/JAS3818.1.

——, Y. Yao, and A. Dai, 2015: Decadal relationship between European blocking and North Atlantic Oscillation during 1978–2011. Part I: Atlantic conditions. *J. Atmos. Sci.*, **72**, 1152–1173, doi:10.1175/JAS-D-14-0039.1.

——, Y. Xiao, Y. Diao, A. Dai, C. Franzke, and I. Simmonds, 2016: Impact of Ural blocking on winter warm Arctic–cold Eurasian anomalies. Part II: The link to the North Atlantic Oscillation. *J. Climate*, **29**, 3949–3971, doi:10.1175/JCLI-D-15-0612.1.

Magnusdottir, G., C. Deser, and R. Saravanan, 2004: The effects of North Atlantic SST and sea ice anomalies on the winter circulation in CCM3. Part I: Main features and storm track characteristics of the response. *J. Climate*, **17**, 857–876, doi:10.1175/1520-0442(2004)017<0857:TEONAS>2.0.CO;2.

Mori, M., M. Watanabe, H. Shiogama, J. Inoue, and M. Kimoto, 2014: Robust arctic sea-ice influence on the frequent Eurasian cold winters in past decades. *Nat. Geosci.*, **7**, 869–873, doi:10.1038/ngeo2277.

Murray, R. J., and I. Simmonds, 1995: Responses of climate and cyclones to reductions in arctic winter sea ice. *J. Geophys. Res.*, **100**, 4791–4806, doi:10.1029/94JC02206.

Nakanowatari, T., K. Sato, and J. Inoue, 2014: Predictability of the Barents Sea ice in early winter: Remote effects of oceanic and

atmospheric thermal conditions from the North Atlantic. *J. Climate*, **27**, 8884–8901, doi:10.1175/JCLI-D-14-00125.1.

Newson, R. L., 1973: Response of general circulation model of the atmosphere to removal of the arctic ice cap. *Nature*, **241**, 39–40, doi:10.1038/241039b0.

Overland, J., K. R. Wood, and M. Wang, 2011: Warm Arctic-cold continents: Climate impacts of the newly open arctic sea. *Polar Res.*, **30**, 15787, doi:10.3402/polar.v30i0.15787.

Park, D. S., S. Lee, and S. Feldstein, 2015: Attribution of the recent winter sea ice decline over the Atlantic sector of the Arctic Ocean. *J. Climate*, **28**, 4027–4033, doi:10.1175/JCLI-D-15-0042.1.

Parkinson, C. L., D. J. Cavalieri, P. Gloersen, H. J. Zwally, and J. Comiso, 1999: Arctic sea ice extents, areas, and trends, 1978–1996. *J. Geophys. Res.*, **104**, 20 837–20 856, doi:10.1029/1999JC900082.

Peings, Y., and G. Magnusdottir, 2014: Forcing of the wintertime atmospheric circulation by the multidecadal fluctuations of the North Atlantic Ocean. *Environ. Res. Lett.*, **9**, 034018, doi:10.1088/1748-9326/9/3/034018.

Petoukhov, V., and V. A. Semenov, 2010: A link between reduced Barents-Kara sea ice and cold winter extremes over northern continents. *J. Geophys. Res.*, **115**, D21111, doi:10.1029/2009JD013568.

Sato, K., J. Inoue, and M. Watanabe, 2014: Influence of the Gulf Stream on the Barents Sea ice retreat and Eurasian coldness during early winter. *Environ. Res. Lett.*, **9**, 084009, doi:10.1088/1748-9326/9/8/084009.

Screen, J. A., and I. Simmonds, 2010: The central role of diminishing sea ice in recent arctic temperature amplification. *Nature*, **464**, 1334–1337, doi:10.1038/nature09051.

——, and ——, 2013a: Exploring links between arctic amplification and mid-latitude weather. *Geophys. Res. Lett.*, **40**, 959–964, doi:10.1002/grl.50174.

——, and ——, 2013b: Caution needed when linking weather extremes to amplified planetary waves. *Proc. Natl. Acad. Sci. USA*, **110**, E2327, doi:10.1073/pnas.1304867110.

——, and ——, 2014: Amplified mid-latitude planetary waves favour particular regional weather extremes. *Nat. Climate Change*, **4**, 704–709, doi:10.1038/nclimate2271.

——, ——, C. Deser, and R. Tomas, 2013: The atmospheric response to three decades of observed arctic sea ice loss. *J. Climate*, **26**, 1230–1248, doi:10.1175/JCLI-D-12-00063.1.

——, C. Deser, I. Simmonds, and R. Tomas, 2014: Atmospheric impacts of arctic sea-ice loss, 1979–2009: Separating forced change from atmospheric internal variability. *Climate Dyn.*, **43**, 333–344, doi:10.1007/s00382-013-1830-9.

Seierstad, I. A., and J. Bader, 2009: Impact of a projected future arctic sea ice reduction on extratropical storminess and the NAO. *Climate Dyn.*, **33**, 937–943, doi:10.1007/s00382-008-0463-x.

Serreze, M. C., M. M. Holland, and J. Stroeve, 2007: Perspectives on the Arctic's shrinking sea-ice cover. *Science*, **315**, 1533–1536, doi:10.1126/science.1139426.

Simmonds, I., 2015: Comparing and contrasting the behaviour of arctic and Antarctic sea ice over the 35 year period 1979–2013. *Ann. Glaciol.*, **56**, 18–28, doi:10.3189/2015AoG69A909.

——, and P. D. Govekar, 2014: What are the physical links between arctic sea ice loss and Eurasian winter climate. *Environ. Res. Lett.*, **9**, 101003, doi:10.1088/1748-9326/9/10/101003.

Spielhagen, R. F., and Coauthors, 2011: Enhanced modern heat transfer to the Arctic by warm Atlantic water. *Science*, **331**, 450–453, doi:10.1126/science.1197397.

Tang, Q., X. Zhang, X. Yang, and J. A. Francis, 2013: Cold winter extremes in northern continents linked to arctic sea ice loss. *Environ. Res. Lett.*, **8**, 014036, doi:10.1088/1748-9326/8/1/014036.

Tibaldi, S., and F. Molteni, 1990: On the operational predictability of blocking. *Tellus*, **42A**, 343–365, doi:10.1034/j.1600-0870.1990.t01-2-00003.x.

Vihma, T., 2014: Effects of arctic sea ice decline on weather and climate. *Surv. Geophys.*, **35**, 1175–1214, doi:10.1007/s10712-014-9284-0.

Walsh, J. E., 2014: Intensified warming of the Arctic: Causes and impacts on middle latitudes. *Global Planet. Change*, **117**, 52–63, doi:10.1016/j.gloplacha.2014.03.003.

Wu, B. Y., D. R. Handorf, K. Dethloff, A. Rinke, and A. X. Hu, 2013: Winter weather patterns over northern Eurasia and arctic sea ice loss. *Mon. Wea. Rev.*, **141**, 3786–3800, doi:10.1175/MWR-D-13-00046.1.

Zhang, X., C. Lu, and Z. Guan, 2012: Weakened cyclones, intensified anticyclones and recent extreme cold winter weather events in Eurasia. *Environ. Res. Lett.*, **7**, 044044, doi:10.1088/1748-9326/7/4/044044.